Molecular and Electronic Structures of Bis(pyridine-2,6-diimine)metal Complexes [ML$_2$](PF$_6$)$_n$ (*n* = 0, 1, 2, 3; M = Mn, Fe, Co, Ni, Cu, Zn)[†]

Bas de Bruin, Eckhard Bill, Eberhard Bothe, Thomas Weyhermüller, and Karl Wieghardt*

Max-Planck-Institut für Strahlenchemie, Stiftstrasse 34-36, D-45470 Mülheim an der Ruhr, Germany

Received February 3, 2000

A series of mononuclear, octahedral first-row transition metal ion complexes *mer*-[M^{II}L$^0_2$](PF$_6$)$_2$ containing the tridentate neutral ligand 2,6-bis[1-(4-methoxyphenylimino)ethyl]pyridine (L^0) and a Mn^{II}, Fe^{II}, Co^{II}, Ni^{II}, Cu^{II}, or Zn^{II} ion have been synthesized and characterized by X-ray crystallography. Cyclic voltammetry and controlled potential coulometry show that each dication (except those of Cu^{II} and Zn^{II}) can be reversibly one-electron-oxidized, yielding the respective trications [M^{III}L$^0_2$]$^{3+}$, and in addition, they can be reversibly reduced to the corresponding monocations [ML$_2$]$^+$ and the neutral species [ML$_2$]^0 by two successive one-electron processes. [MnL$_2$]PF$_6$ and [CoL$_2$]PF$_6$ have been isolated and characterized by X-ray crystallography; their electronic structures are described as [Mn^{III}L$^1_2$]PF$_6$ and [Co^{I}L$^0_2$]PF$_6$ where (L^1)$^{1-}$ represents the one-electron-reduced radical form of L^0. The electronic structures of the tri-, di-, and monocations and of the neutral species have been elucidated in detail by a combination of spectroscopies: UV−vis, NMR, X-band EPR, Mössbauer, temperature-dependent magnetochemistry. It is shown that pyridine-2,6-diimine ligands are noninnocent ligands that can be coordinated to transition metal ions as neutral L^0 or, alternatively, as monoanionic radical (L^1)$^{1-}$. All trications are of the type [M^{III}L$^0_2$]$^{3+}$, and the dications are [M^{II}L$^0_2$]$^{2+}$. The monocations are described as [Mn^{III}L$^1_2$]$^+$ (*S* = 0), [Fe^{II}L^{0}L^1]$^+$ (*S* = $^1/_2$), [Co^{I}L$^0_2$]$^+$ (*S* = 1), [Ni^{II}L$^0_2$]$^+$ (*S* = $^1/_2$), [Cu^{I}L$^0_2$]$^+$ (*S* = 0), [Zn^{II}L^{1}L^0]$^+$ (*S* = $^1/_2$) where the Mn^{III} and Fe^{II} ions are low-spin-configurated. The neutral species are described as [Mn^{II}L$^1_2$]^0, [Fe^{II}L$^1_2$]^0, [Co^{I}L^{0}L^1]^0, [Ni^{I}L^{0}L^1]^0, and [Zn^{II}L$^1_2$]^0; their electronic ground states have not been determined.
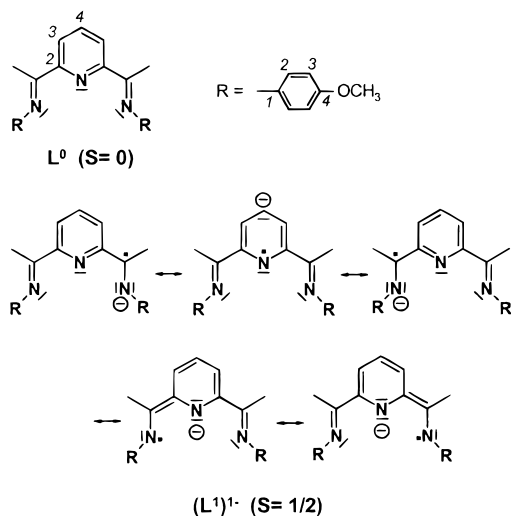
Introduction

Werner-type coordination chemistry of classic tridentate nitrogen donor ligands with transition metal ions has in recent years been revitalized because of the rather unexpected discovery that complexes of this type are very active olefin polymerization catalysts. In particular, the pyridine-2,6-diimine (L) ligands as 2,2′:6,2″-terpyridine analogues and their iron and cobalt complexes have shown spectacular results in this respect.[1] Brookhart et al. also reported recently (pyridine-2,6-diimine)-ruthenium complexes that catalyze the epoxidation of olefins,[2] whereas Vrieze et al.[3] reported an interesting stoichiometric reaction of an α-chlorotolyl(pyridine-2,6-diimine)rhodium complex with H$_2$O and O$_2$ to give benzylaldehyde and H$_2$O$_2$. Electrocatalytic reduction of CO$_2$ with [CoL$_2$](PF$_6$)$_2$ and [NiL$_2$]-(PF$_6$)$_2$ complexes as catalysts has also been reported.[4] L represents in this instance 2,6-bis[1-(phenylimino)ethyl]pyridine. The "reduced forms" of complexes are assumed to be the ones that are active in the electrocatalytic process. These forms had not been further characterized.

Most complexes prepared to date are either five-coordinate [M^{II}X$_2$(L^0)] (M = Mn, Fe, Co, Ni, Cu, Zn, Cd; X = Cl, Br) or six-coordinate species [M^{II}L$^0_2$]X$_2$ containing one or two neutral, tridentate meridionally coordinated L^0 ligands.[5−17] In all cases these neutral, coordinated ligands have been described to be redox-innocent and the oxidation state of the central metal ion has been calculated accordingly. This approach is shown here to be somewhat simplistic and may yield an incorrect description of the true electronic structure of a given complex in view of the observation that all [ML$^0_2$]$^{2+}$ complexes display a rich redox chemistry where at least two reversible one-electron reductions and, in addition, quite often a reversible one-electron oxidation are observed. In earlier work Toma et al.[14,15] have employed spectroelectrochemical methods to characterize the reduced and

† Dedicated to Professor Heinrich Vahrenkamp on the occasion of his 60th birthday.

(1) (a) Small, B. L.; Brookhart, M. *Macromolecules* **1999**, *32*, 2120. (b) Britovsek, G. J. P.; Bruce, M.; Gibson, V. C.; Kimberley, B. S.; Maddox, P. J.; Mastroianni, S.; McTavish, S. J.; Redshaw, C.; Solan, G. A.; Strömberg, S.; White, A. J. P.; Williams, D. J. *J. Am. Chem. Soc.* **1999**, *121*, 8728. (c) Small, B. L.; Brookhart, M.; Bennett, A. M. A. *J. Am. Chem. Soc.* **1998**, *120*, 4049. (d) Britovsek, G. J. P.; Gibson, V. C.; Kimberley, B. S.; Maddox, P. J.; McTavish, S. J.; Solan, G. A.; White, A. J. P.; Williams, D. J. *Chem. Commun.* **1998**, 849.

(2) Cetinkaya, B.; Cetinkaya, E.; Brookhart, M.; White, P. S. *J. Mol. Catal. A* **1999**, *142*, 101.

(3) Haarman, H. F.; Bregman, F. R.; van Leeuwen, P. W. N. M.; Vrieze, K. *Organometallics* **1997**, *16*, 979.

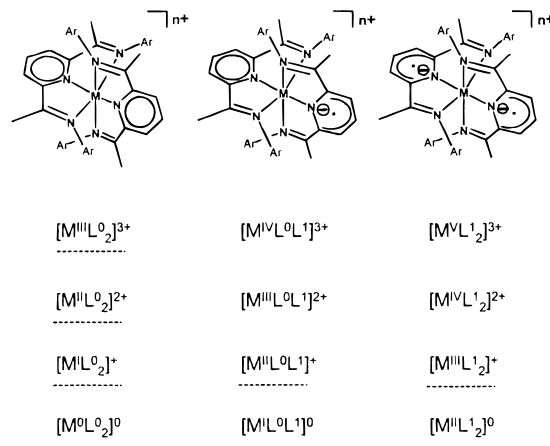(4) Arana, C.; Yau, S.; Keshavarz, K. M.; Potts, K. T.; Abruna, H. D. *Inorg. Chem.* **1992**, *31*, 3680.

(5) Alyea, E. C.; Merrell, P. H. *Synth. React. Inorg. Met.−Org. Chem.* **1974**, *4*, 535.

(6) Alyea, E. C.; Ferguson, G.; Restivo, R. J. *Inorg. Chem.* **1975**, *14*, 2491.

(7) Alyea, E. C.; Ferguson, G.; Restivo, R. J.; Merrell, P. H. *J. Chem. Soc., Chem. Commun.* **1975**, 269.

(8) Alyea, E. C.; Merrell, P. H. *Inorg. Chim. Acta* **1978**, *28*, 91.

(9) Merrell, P. H.; Alyea, E. C.; Ecott, L. *Inorg. Chim. Acta* **1982**, *59*, 25.

(10) Alyea, E. C. *Inorg. Chim. Acta* **1983**, *76*, L239.

(11) Restivo, R. J.; Ferguson, G. *J. Chem. Soc., Dalton Trans.* **1976**, 518.

(12) Edwards, D. A.; Mahon, M. F.; Martin, W. R.; Molloy, K. C.; Fanwick, P. E.; Walton, R. A. *J. Chem. Soc., Dalton Trans.* **1990**, 3161.

(13) Edwards, D. A.; Edwards, S. D.; Martin, W. R.; Pringle, T. J.; Thornton, P. *Polyhedron* **1992**, *11*, 1569.

(14) Kuwabara, I. H.; Comninos, F. C. M.; Pardini, V. L.; Viertler, H.; Toma, H. E. *Electrochim. Acta* **1994**, *39*, 2401 and references therein.

(15) Toma, H. E.; Chavez-Gil, T. E. *Inorg. Chim. Acta* **1997**, *257*, 197 and references therein.

(16) Stor, G. J.; van der Vis, M.; Stufkens, D. J.; Oskam, A. *J. Organomet. Chem.* **1994**, *482*, 15.

(17) Marcos, D.; Folgado, J.-V.; Beltran-Porter, D.; do Prado-Gambardella, M. T.; Pulcinelli, S. H.; deAlmeida-Santos, R. H. *Polyhedron* **1990**, *9*, 2699.

Scheme 1. Resonance Structures of the L^0 and $(L^1)^{1-}$ Ligands

Scheme 2. Possible Oxidation Level Distribution of Ligands and Metal Ions in Tri-, Di-, and Monocations and in the Neutral Species $[ML_2]^{n+}$ ($n = 3, 2, 1, 0$)

The dotted lines indicate species characterized in this work

oxidized forms of $[Fe^{II}L^0_2]^{2+}$ complexes but have not provided definitive evidence for the electronic structures of these species. In other words, metal vs ligand-centered reductions (or oxidations) must be carefully considered. For example, this problem has been addressed in the chemistry of $[M(bpy)_3]^{n+}$,[19] [M-(terpy)_2]^{n+}$, [20] and $[M(diimine)_3]^{n+}$ [21] complexes ($n = 3, 2, 1$, 0). Recently, an example for bidentate coordination of a pyridine-2,6-bis(imine) ligand has been provided in *fac*-[ReCl-(CO)_3L^0]. [18]

In this work we show that octahedral complexes $[ML_2]^{n+}$ of the ligand 2,6-bis[1-(4-methoxyphenylimino)ethyl]pyridine[5,22] and a first-row transition metal ion (M = Mn, Fe, Co, Ni, Cu, Zn) can exist as tri-, di-, or monocations and even as neutral complexes $[ML_2]^0$. For each complex we will carefully address the question of the actual oxidation level of the ligands that can be coordinated as a neutral ligand L^0 or as radical monoanion $(L^1)^{1-}$. Scheme 1 gives a number of resonance structures for both forms, which are taken as a first rough indication of structural changes within the ligand that might be expected when L^0 is one-electron-reduced to $(L^1)^{1-}$. In principle, it is conceivable that the tri-, di-, and monocations and the neutral species $[ML_2]^{n+}$ ($n = 3, 2, 1, 0$) can each adopt one of three electronic structures shown in Scheme 2 depending on the oxidation level of the two ligands and the central metal ion.

We have chosen the *p*-methoxy derivative of the pyridine-2,6-diimines because it is synthetically readily accessible[5] and because the crystallinity of $[ML_2]^{n+}$ complexes ($n = 2, 1$) was found to be superior in comparison to other aryl derivatives. In addition, the uncoordinated L^0 ligand has been structurally

characterized by X-ray crystallography.[22] The present work clearly demonstrates that these pyridine-2,6-diimine ligands are noninnocent.

The following species have been synthesized and spectroscopically partially characterized previously: $[MnL^0_2](ClO_4)_2$ [12] and $[Co^{II}L^0_2](ClO_4)_2$.[13] Note that in the following we will use the designation L for the ligand $C_{23}H_{23}N_3O_2$ with unspecified overall charge or oxidation level, where L^0 represents the diamagnetic, neutral ligand $[C_{23}H_{23}N_3O_2]^0$ and $(L^1)^{1-}$ is its monoanionic radical $[C_{23}H_{23}N_3O_2]^{1-}$ (Scheme 1).

Synthesis and Characterization

The reaction of 2 equiv of the neutral, tridentate ligand 2,6-bis[1-(4-methoxyphenylimino)ethyl]pyridine (L^0) with 1 equiv of an appropriate metal(II) salt in methanol yields octahedral dications $[ML_2]^{2+}$ (M = Mn, Fe, Co, Ni, Cu, Zn) of which the hexafluorophosphate salts have been isolated as crystalline solids by addition of excess $[NH_4]PF_6$.

The corresponding monocationic species $[ML_2]PF_6$ (M = Mn, Co) have been generated and isolated as crystalline solids by one-electron reduction of the corresponding dication with 1 equiv of cobaltocene in acetonitrile solution under an argon blanketing atmosphere. These are the first isolated $[ML_2]X$ salts.

From temperature-dependent susceptibility measurements (2–298 K) using a superconducting quantum interference device (SQUID) magnetometer we have determined the magnetic moments of complexes. Complexes $[ML_2](PF_6)_2$ (M = Fe, Zn) and $[MnL_2]PF_6$ are diamagnetic; they possess a singlet ground state ($S = 0$). All other species are paramagnetic. Their magnetic moments as a function of the temperature are shown in Figure 1. Orange-red $[MnL_2](PF_6)_2$ exhibits a nearly temperature-independent magnetic moment of 5.90 μ_B at 10 K and 6.02 μ_B at 290 K, close to the expected value of 5.92 μ_B for an $S = 5/2$ system. From the susceptibility data we derive $g = 2.005$, $|D| = 0.12$ cm^{-1} and a temperature-independent paramagnetism, χ_{TIP}, of 463×10^{-6} cm^3 mol^{-1} indicative of a high-spin manganese(II) ion. Similar results have been reported previously for the perchlorate salt.[12] Thus, this species contains two neutral L^0 ligands: $[Mn^{II}L^0_2](PF_6)_2$.

The nearly temperature-independent magnetic moments of 1.81 μ_B at 4 K and 1.91 μ_B at 298 K indicate an $S = 1/2$ ground state for $[CoL_2](PF_6)_2$. In contrast, previous authors[13] have reported an $S = 3/2$ ground state for the corresponding

(18) Granifo, J.; Bird, S. J.; Orrell, K. G.; Osborne, A. G.; Sik, V. *Inorg. Chim. Acta* **1999**, *295*, 56.

(19) Perez-Cordero, E.; Buigas, R.; Brady, N.; Eschegoyen, L.; Arana, C.; Lehn, J.-M. *Helv. Chim. Acta* **1994**, *77*, 1222. (b) Eschegoyen, L.; De Cian, A.; Fischer, J.; Lehn, J.-M. *Angew. Chem., Int. Ed. Engl.* **1991**, *30*, 838. (c) Perez-Cordero, E. E.; Campana, C.; Eschegoyen, L. *Angew. Chem., Int. Ed. Engl.* **1997**, *36*, 137.

(20) (a) Berger, R. M.; McMillin, D. R. *Inorg. Chem.* **1988**, *27*, 4245. (b) Morris, D. E.; Hanck, K. W.; DeArmond, M. K. *J. Electroanal. Chem.* **1983**, *149*, 115. (c) Pyo, S.; Perez-Cordero, E.; Bott, S. G.; Eschegoyen, L. *Inorg. Chem.* **1999**, *38*, 3337.

(21) (a) Gagne, R. R.; Ingle, D. M. *Inorg. Chem.* **1981**, *20*, 420. (b) Vrieze, K.; van Koten, G. *Inorg. Chim. Acta* **1985**, *100*, 79. (c) van Koten, G.; Jastrzebski, J. T. B. H.; Vrieze, K. *J. Organomet. Chem.* **1983**, *250*, 49. (d) Dieck, H. T.; Franz, K.-D.; Hohmann, F. *Chem. Ber.* **1975**, *108* (1), 163.

(22) Meehan, P. R.; Alyea, E. C.; Ferguson, G. *Acta Crystallogr., Sect. C: Cryst. Struct. Commun.* **1997**, *53*, 888.
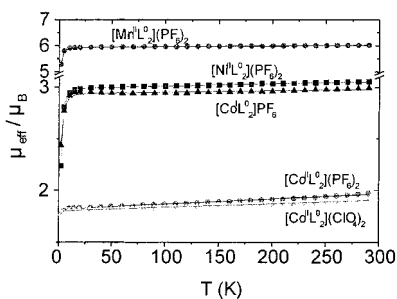
Figure 1. Temperature-dependent magnetic moments, μ_{eff}, μ_B, of complexes. The solid lines represent best fits using parameters given in the text.
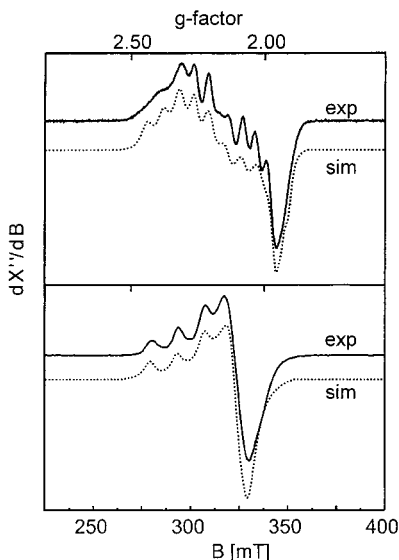

Figure 2. Top: X-band EPR spectrum of $[Co^{II}L^0{}_2](PF_6)_2$ in CH$_3$CN at 10 K. Conditions are the following: frequency, 9.6463 GHz; microwave power, 1 μW; modulation amplitude, 1.25 mT. Bottom: X-band EPR spectrum of $[Cu^{II}L^0{}_2](PF_6)_2$ in CH$_3$CN at 10 K. Conditions are the following: frequency, 9.4346 GHz; microwave power, 1 μW; modulation amplitude, 1.25 mT. The simulations were obtained with parameters given in the text.

Table 1. NMR Data for the Diamagnetic Compounds[a]

	$L^{0\,b}$	$[Zn^{II}L^0{}_2](PF_6)_2{}^c$	$[Mn^{III}L^1{}_2]PF_6{}^c$	$[Fe^{II}L^0{}_2](PF_6)_2{}^c$
		^{1}H NMR		
Py−H3 (^3J(H,H))	8.29 (7.8)	8.20 (7.3)	7.84 (7.6)	8.05−8.15
Py−H4 (^3J(H,H))	7.94 (7.8)	8.40 (7.3)	7.41 (7.6)	8.05−8.15
−OCH$_3$	3.80	3.71	3.60	3.68
−CH$_3$	2.40	2.41	2.47	2.54
Ph−H2 (^3J(H,H))	6.95 (8.8)	6.72 (8.9)	6.45 (8.1)	6.66 (8.8)
Ph−H3 (^3J(H,H))	6.82 (8.8)	6.41 (8.9)	5.64 (8.1)	6.08 (8.8)
		^{13}C NMR		
Py−C2	155.7	159.4	158.2	160.3
Py−C3	122.1	128.5	121.6	127.7
Py−C4	136.7	138.0	124.0	136.6
$C=$N	167.4	168.2	167.2	179.2
−CH$_3$	16.1	17.8	17.4	19.4
−OCH$_3$	55.5	56.2	56.1	56.3
Ph−C1	144.4	145.8	140.7	137.7
Ph−C2	120.9	122.8	122.0	121.8
Ph−C3	114.2	115.6	114.3	115.6
Ph−C4	156.3	148.1	150.9	159.7

[a] The signals (δ (ppm), J (Hz)) are assigned using the numbering in Scheme 1. [b] ^{1}H NMR spectrum recorded in CD$_3$CN, ^{13}C NMR spectrum recorded in CDCl$_3$. [c] ^{1}H NMR and ^{13}C NMR spectra recorded in CD$_3$CN.

likely because of the unfavorable orientation of the $e_g{}^1$ and π^{*1} orbitals for ferromagnetic coupling. Furthermore, the observed zero-field splitting $|D| = 3.4$ for $[Co^IL^0{}_2]PF_6$ is very similar to $|D| = 4.5$ cm^{-1} for the isoelectronic $[Ni^{II}L^0{}_2](PF_6)_2$.

Similarly, a nearly temperature-independent magnetic moment of 2.87 μ_B of $[NiL_2](PF_6)_2$ is indicative of an octahedral nickel-(II) ion ($S = 1$). From the temperature-dependent susceptibility data we derive the parameters $g = 2.11$, $|D| = 4.5$ cm^{-1}, and $\chi_{TIP} = 175 \times 10^{-6}$ cm^3 mol^{-1}, in agreement with the electronic structure of $[Ni^{II}L^0{}_2](PF_6)_2$. Note that the cations in $[Co^IL^0{}_2]$-PF$_6$ and $[Ni^{II}L^0{}_2](PF_6)_2$ are isostructural and isoelectronic, both containing a metal ion with a high-spin d^8 electron configuration.

The complex $[Cu^{II}L^0{}_2](PF_6)_2$ displays a nearly temperature-independent magnetic moment of 1.82 μ_B at 10 K and 1.88 μ_B at 298 K. From the susceptibility data we derived the parameters $g = 2.097$ and $\chi_{TIP} = 100 \times 10^{-6}$ cm^3 mol^{-1}, indicative of an octahedral Cu^{II} (d^9) complex (Figure S1 of Supporting Information). From its X-band EPR spectrum in CH$_3$CN solution at 10 K (Figure 2, bottom) the following parameters were derived: $g_\perp = 2.087$, $g_\parallel = 2.245$, $A_\parallel = 145 \times 10^{-4}$ cm^{-1}, $A_\perp =$ unresolved.

Surprisingly, the dark-blue complex $[MnL_2]PF_6$ possesses an $S = 0$ ground state. From temperature-dependent susceptibility measurements small effective magnetic moments of 1.29 μ_B at 290 K and 0.88 μ_B at 8 K were measured. We obtained a satisfactory fit of the magnetic susceptibility data with $\chi_{TIP} = 390 \times 10^{-6}$ cm^3 mol^{-1} and 3% of a paramagnetic impurity ($S = \frac{5}{2}$).

The diamagnetic complexes $[ZnL_2](PF_6)_2$, $[MnL_2]PF_6$, and $[FeL_2](PF_6)_2$ dissolved in CD$_3$CN solution at ambient temperature display ^{1}H and ^{13}C NMR signals in the normal range for diamagnetic compounds. Table 1 summarizes these data. The spectra reveal that the two ligands of the $[ML_2]^{n+}$ cations are equivalent on the NMR time scale and, furthermore, that a given LM fragment is bisected by a (noncrystallographic) mirror plane where the metal ion, the pyridine nitrogen, and a carbon atom in the para position lie on this plane. Although significant shifts of some signals are observed in the ^{1}H and ^{13}C NMR spectra on going from the free L^0 ligand to $[ZnL_2](PF_6)_2$ and to $[MnL_2]$-PF$_6$, it is difficult to distinguish anisotropic shielding/deshielding because of ring current effects from shifts caused by charge
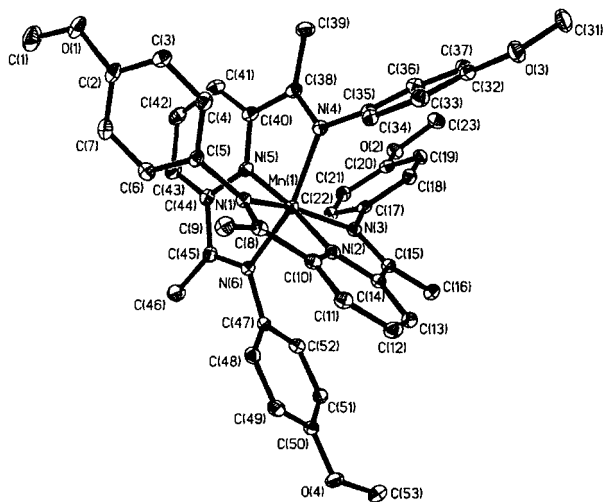
perchlorate salt $[CoL_2](ClO_4)_2$ (μ_{eff} (25 °C) = 4.62 μ_B). We have reexamined this salt and find an $S = \frac{1}{2}$ ground state in the solid state (Figure 1). From the susceptibility data we derive $g = 2.10$, $\chi_{TIP} = 235 \times 10^{-6}$ cm^3 mol^{-1} for the PF$_6$ salt and $g = 2.08$, $\chi_{TIP} = 165 \times 10^{-6}$ cm^3 mol^{-1} for the ClO$_4$ salt. The X-band EPR spectrum of $[CoL_2](PF_6)_2$ in CH$_3$CN at 10 K shown in Figure 2 also confirms the $S = \frac{1}{2}$ ground state of this dication in frozen solution. The rhombic spectrum was successfully simulated with $g_x = 2.221$, $g_y = 2.203$, $g_z = 1.973$ and hyperfine coupling to the ^{59}Co ($I = \frac{7}{2}$) nucleus with $A_{xx} = 24.9 \times 10^{-4}$ cm^{-1}, $A_{yy} = 85.3 \times 10^{-4}$ cm^{-1}, and $A_{zz} =$ unresolved. No resolved superhyperfine coupling to the ^{14}N nuclei has been observed. These data are fully consistent with an electronic structure of $[Co^{II}L^0{}_2]X_2$ containing a low-spin cobalt(II) ion (d^7).

Deep-green $[CoL_2]PF_6$ exhibits a nearly temperature-independent magnetic moment of 2.99−2.96 μ_B in the temperature range 300−20 K. This value is very close to the expected value of 2.83 μ_B for an $S = 1$ system and is indicative of an octahedral cobalt(I) ion in $[Co^IL^0{}_2]PF_6$. From the temperature-dependent susceptibility data we derive the following parameters (Figure 1): $g = 2.09$; $|D| = 3.4$ cm^{-1}. Thus, an electronic structure $[Co^IL^0{}_2]PF_6$ appears to prevail. The description of $[Co^{II}L^1L^0]$-PF$_6$ containing a low-spin Co^{II} ($S = \frac{1}{2}$) strongly ferromagnetically coupled to a ligand radical (L^1)$^{1-}$ ($S = \frac{1}{2}$) is much less

Figure 3. Structure of the monocation in crystals of $[Mn^{III}L^1_2]PF_6$.

accumulation. In general, ring current shielding/deshielding effects are less prominent for ^{13}C NMR signals. Thus, the observed upfield shifts of some of the ^{13}C NMR pyridine signals in $[MnL_2]PF_6$ relative to $[ZnL_2](PF_6)_2$ are indicative of an increased negative charge on this pyridine ring.

The diamagnetic complex $[FeL_2](PF_6)_2$ has been studied by zero-field Mössbauer spectroscopy. At 80 K a symmetrical quadrupole doublet with an isomer shift, δ, of 0.235(8) mm s^{-1} and a quadrupole splitting, ΔE_Q, of 1.081(5) mm s^{-1} has been observed (Figure S2). In comparison, these parameters are $\delta = 0.238$ and $\Delta E_Q = 1.14$ mm s^{-1} for low-spin $[Fe^{II}(terpy)_2]$-$(ClO_4)_2$,[23] whereas for low-spin $[Fe^{III}(terpy)_2](ClO_4)_3$ the values are 0.07 and 3.43 mm s^{-1}.[24] Clearly, the electronic structure of the above complex must be described as $[Fe^{II}L^0_2](PF_6)_2$. On the other hand, for low-spin $[Fe^{II}(bpy)_3](ClO_4)_2$ Mössbauer parameters $\delta = 0.325$, $\Delta E_Q = 0.39$ mm s^{-1} [25] have been reported. The lower isomer shifts of $[Fe^{II}L^0_2](PF_6)_2$ and $[Fe^{II}$-$(terpy)_2](ClO_4)_2$ relative to $[Fe^{II}(bpy)_3](ClO_4)_2$ indicate significant charge delocalization from the metal t_{2g} orbitals into the ligand π^* orbitals via π back-donation. Consistent with this interpretation is the increasing intensity of the metal-to-ligand charge-transfer bands[15] in the visible on going from $[ZnL^0_2]^{2+}$ to $[Mn^{II}L^0_2]^{2+}$ to $[Co^{II}L^0_2]^{2+}$ and, finally, to $[Fe^{II}L^0_2]^{2+}$ (see Figures 5 and 10).

X-ray Structures. Single crystals suitable for X-ray crystallography of orange-red $[MnL_2](PF_6)_2$, dark-blue $[MnL_2]PF_6$, purple-black $[FeL_2](PF_6)_2$, brown-black $[CoL_2](PF_6)_2$, green-black $[CoL_2]PF_6$, brown $[NiL_2](PF_6)_2$, brown $[CuL_2](PF_6)_2$, and yellow $[ZnL_2](PF_6)_2$ were grown from acetonitrile solutions top-layered with diethyl ether.

All structures consist of mono- or dications, $[ML_2]^{+/2+}$, and well-separated hexafluorophosphate anions. The metal ions are in a distorted octahedral environment comprising two meridionally coordinated L ligands that orientate the pyridine nitrogen donors in a mutually trans position. As a representative example, the molecular structure of $[MnL_2]^+$ is shown in Figure 3. Atom labels used here are the same for all structures. Table 2 gives bond distances and angles.

A common feature of all structures is the observation that the metrical details of both coordinated ligands in a given

(23) Epstein, L. M. *J. Chem. Phys.* **1964**, *40*, 435.
(24) Reif, W. M.; Baker, W. A., Jr.,; Erickson, N. E. *J. Am. Chem. Soc.* **1968**, *90*, 4794.
(25) Collins, R. L.; Pettit, R.; Baker, W. A., Jr. *J. Inorg. Nucl. Chem.* **1966**, *28*, 1001.

$[ML_2]^{n+}$ cation are, within experimental error, identical and, furthermore, that, as noted above, the LM fragment is bisected by a noncrystallographic mirror plane, i.e., the two halves of a coordinated L ligand are identical. For the following discussion it therefore suffices to compare the averaged bond distances $C_{py}-N_{py}$, $C_{py}-C_{imine}$, $C_{imine}-N_{imine}$ as summarized in Table 3. The dimensions of the *p*-methoxyphenyl groups do not vary across the series within experimental error.

The compound $[Zn^{II}L^0_2](PF_6)_2$ serves as a benchmark for a redox innocent case where the well-defined oxidation state of the central zinc ion (+II, d^{10}) unequivocally renders the two ligands as L^0 (neutral molecules). Typically, the average $C_{imine}-N_{imine}$ distance at 1.285(2) Å is short and indicates a C=N double bond whereas the average $C_{py}-C_{imine}$ bond length at 1.502(2) Å corresponds to that of a typical C–C single bond. The $C_{py}-N_{py}$ bonds at 1.336(2) Å and the $C_{py}-C_{py}$ distances are equidistant at 1.390(2) Å and indicative of an unperturbed pyridine ring.

As can be seen from the data compiled in Table 3, exactly the same oxidation level of the two ligands in $[MnL^0_2](PF_6)_2$ prevails, namely, L^0. Thus, the electronic structure of this compound must be described as $[Mn^{II}L^0_2](PF_6)_2$ comprising an octahedral high-spin Mn^{II} ion and two neutral L^0 ligands. Similarly, the metrical details of the coordinated ligands in $[Co^{II}L^0_2](PF_6)_2$ are in good agreement with its formulation as neutral L^0 ligands rendering the central metal ion low-spin Co^{II}. However, barely significantly the average $C_{imine}-N_{imine}$ bond at 1.295(2) Å is *longer* by 0.01 Å than in $[ZnL^0_2](PF_6)_2$ and $[MnL^0_2](PF_6)$, the average $C_{py}-C_{imine}$ bond at 1.480(3) Å is *shorter* by 0.022 Å, and the average $C_{py}-N_{py}$ distance is again longer by 0.012 Å than in the two former cases. This trend is augmented on going to $[Fe^{II}L^0_2](PF_6)_2$, which, according to the Mössbauer spectrum and magnetic susceptibility measurements, contains a low-spin ferrous ion. The average $C_{imine}-N_{imine}$ is again slightly elongated, whereas the average $C_{py}-C_{imine}$ bond is shortened and the $C_{py}-N_{py}$ distances are elongated in comparison with the $[Zn^{II}L^0_2](PF_6)_2$ and $[Mn^{II}L^0_2](PF_6)_2$ species. The metrical details of the ligands in $[CoL_2]PF_6$, $[NiL_2](PF_6)_2$ and $[CuL_2](PF_6)_2$ are between those of $[Fe^{II}L^0_2](PF_6)_2$ and $[ZnL^0_2](PF_6)_2$. Consequently, we assign the following oxidation levels: $[Co^IL^0_2]PF_6$ containing an octahedral cobalt(I) ion (d^8), $[Ni^{II}L^0_2](PF_6)_2$ with an isoelectronic nickel(II) ion, and $[Cu^{II}L^0_2]$-$(PF_6)_2$ containing an octahedral copper(II) ion (d^9).

It is now significant and quite remarkable that in $[MnL_2]PF_6$ the *longest* average $C_{imine}-N_{imine}$ bond length at 1.321(2) Å, the *shortest* average $C_{py}-C_{imine}$ bond at 1.442(2) Å, the *longest* $C_{py}-N_{py}$ bonds at 1.373(2) Å of the whole series are observed. The extremes are depicted in Scheme 3 where the ligand dimensions in $[Mn^{II}L^0_2](PF_6)_2$ and its one-electron-reduced form, $[MnL_2]PF_6$, are shown. We take this as an indication that in $[MnL_2]PF_6$ the ligands are coordinated as monoanionic radicals $(L^1)^{1-}$ that would render the central metal ion a low-spin Mn^{III} ion ($S = 1$).

Interestingly, the structure of the octahedral diamagnetic complex $[Mn^I(dapa)(CO)_2Br]$ has been reported[16] where dapa is 2,6-diacetylpyridine-bis(anil) which is an analogue of our L^0 ligand without the *p*-methoxy groups. According to the reported dimensions, the ligand is of the L^0 type with short C=N$_{imine}$ bonds (av 1.288(6) Å), which resembles in this respect the situation in $[Mn^{II}L^0_2](PF_6)_2$ but not $[MnL_2]PF_6$. Thus, we cannot describe the electronic structure as $[Mn^IL^0_2]PF_6$ containing a low-spin Mn^I ion.

Now we turn to the MN_6 octahedra of complexes. For $[Zn^{II}L^0_2](PF_6)_2$ and $[Mn^{II}L^0_2](PF_6)_2$ containing a spherical Zn^{II}

Table 2. Selected Bond Distances (Å) and Bond Angles (deg) of Complexes

	$[Mn^{II}L^0_2]^{2+}$	$[Mn^{III}L^1_2]^+$	$[Fe^{II}L^0_2]^{2+}$	$[Co^{II}L^0_2]^{2+}$	$[Co^{I}L^0_2]^+$	$[Ni^{II}L^0_2]^{2+}$	$[Cu^{II}L^0_2]^{2+}$	$[Zn^{II}L^0_2]^{2+}$
				Bond Distance				
				$M-N_{Py}$				
N2−M1	2.177(2)	1.8867(12)	1.8707(14)	1.852(2)	1.986(5)	1.973(2)	1.9419(11)	2.0369(10)
N5−M1	2.171(2)	1.8832(12)	1.8655(14)	1.991(2)	1.993(5)	1.965(2)	1.9561(11)	2.0464(10)
				$Mn-N_{imine}$				
N1−M1	2.277(2)	1.9831(13)	1.974(2)	2.009(2)	2.153(5)	2.113(2)	2.1588(11)	2.1997(11)
N3−M1	2.249(2)	1.9720(13)	1.999(2)	2.021(2)	2.158(4)	2.134(2)	2.1626(11)	2.2051(10)
N4−M1	2.274(2)	1.9988(12)	1.9817(14)	2.145(2)	2.136(5)	2.129(2)	2.2331(11)	2.1893(11)
N6−M1	2.253(3)	1.9831(12)	1.9922(14)	2.165(2)	2.134(5)	2.134(2)	2.2133(11)	2.2003(12)
				$C_{imine}-N_{imine}$				
N1−C8	1.281(4)	1.319(2)	1.306(2)	1.298(3)	1.294(7)	1.286(3)	1.284(2)	1.282(2)
N3−C15	1.283(4)	1.323(2)	1.309(2)	1.305(3)	1.300(7)	1.295(3)	1.292(2)	1.283(2)
N4−C38	1.284(4)	1.323(2)	1.311(2)	1.289(3)	1.307(7)	1.288(3)	1.283(2)	1.284(2)
N6−C45	1.283(4)	1.320(2)	1.311(2)	1.289(3)	1.310(7)	1.291(3)	1.284(2)	1.290(2)
				$C_{Py}-C_{imine}$				
C8−C10	1.496(5)	1.442(2)	1.466(2)	1.472(4)	1.477(7)	1.492(3)	1.490(2)	1.502(2)
C14−C15	1.500(4)	1.441(2)	1.466(2)	1.476(3)	1.456(8)	1.495(3)	1.496(2)	1.505(2)
C38−C40	1.499(4)	1.440(2)	1.466(2)	1.487(3)	1.455(8)	1.488(3)	1.501(2)	1.499(2)
C44−C45	1.497(4)	1.443(2)	1.470(2)	1.485(3)	1.470(9)	1.493(3)	1.497(2)	1.500(2)
				$N_{Py}-C_{Py}$				
N2−C10	1.335(4)	1.373(2)	1.356(2)	1.347(3)	1.353(7)	1.339(3)	1.338(2)	1.339(2)
N2−C14	1.338(4)	1.373(2)	1.351(2)	1.350(3)	1.363(7)	1.341(3)	1.344(2)	1.336(2)
N5−C40	1.339(4)	1.371(2)	1.355(2)	1.347(3)	1.348(8)	1.343(3)	1.342(2)	1.336(2)
N5−C44	1.341(4)	1.375(2)	1.351(2)	1.350(3)	1.364(7)	1.341(3)	1.347(2)	1.334(2)
				$C_{Py}-C_{Py}$				
C10−C11	1.392(4)	1.390(2)	1.388(2)	1.387(3)	1.384(8)	1.385(3)	1.393(2)	1.384(2)
C11−C12	1.384(5)	1.391(2)	1.386(3)	1.389(4)	1.377(8)	1.387(3)	1.391(2)	1.387(2)
C12−C13	1.385(5)	1.396(2)	1.398(3)	1.385(4)	1.396(8)	1.387(3)	1.392(2)	1.385(2)
C13−C14	1.392(4)	1.390(2)	1.386(3)	1.393(3)	1.391(8)	1.389(3)	1.392(2)	1.393(2)
C40−C41	1.386(4)	1.394(2)	1.383(2)	1.381(3)	1.399(8)	1.385(3)	1.394(2)	1.393(2)
C41−C42	1.381(5)	1.390(2)	1.386(3)	1.389(4)	1.377(8)	1.383(3)	1.386(2)	1.388(2)
C42−C43	1.382(5)	1.390(2)	1.389(3)	1.387(4)	1.379(8)	1.386(3)	1.383(2)	1.392(2)
C43−C44	1.396(4)	1.392(2)	1.397(2)	1.393(3)	1.385(8)	1.390(3)	1.389(2)	1.394(2)
				Bond Angle				
N1−M1−N2	71.74(9)	77.92(5)	79.81(6)	80.17(8)	74.9(2)	77.57(7)	77.65(4)	75.69(4)
N1−M1−N3	143.25(9)	156.31(5)	159.69(6)	160.56(8)	151.0(2)	155.26(7)	155.62(4)	150.92(4)
N1−M1−N4	89.17(9)	92.12(5)	88.59(6)	87.60(8)	98.2(2)	88.07(7)	98.01(4)	88.49(4)
N1−M1−N5	102.47(9)	98.19(5)	99.05(6)	98.52(8)	97.7(2)	101.32(7)	100.78(4)	103.30(4)
N1−M1−N6	100.14(9)	95.27(5)	97.79(6)	97.79(8)	87.3(2)	98.73(7)	87.43(4)	101.01(4)
N2−M1−N3	72.06(9)	78.53(5)	79.89(6)	80.42(8)	76.2(2)	77.73(7)	78.16(4)	75.24(4)
N2−M1−N4	99.42(9)	106.20(5)	99.70(6)	100.97(8)	110.7(2)	101.44(7)	104.50(4)	103.25(4)
N2−M1−N5	169.56(9)	173.78(5)	178.80(6)	178.48(8)	170.7(2)	178.55(7)	178.28(5)	178.50(4)
N2−M1−N6	116.74(9)	97.37(5)	101.03(6)	103.46(8)	98.4(2)	103.86(7)	101.93(4)	105.62(4)
N3−M1−N4	102.76(9)	91.94(5)	94.75(6)	97.11(8)	89.8(2)	98.26(7)	85.11(4)	99.13(4)
N3−M1−N5	114.27(9)	105.49(5)	101.25(6)	100.91(8)	111.3(2)	103.40(7)	103.45(4)	105.78(4)
N3−M1−N6	90.48(9)	90.27(5)	86.16(6)	85.73(8)	99.2(2)	85.75(6)	100.53(4)	85.82(4)
N4−M1−N5	71.44(9)	78.64(5)	79.86(6)	78.16(8)	75.4(2)	77.54(7)	76.36(4)	75.56(4)
N4−M1−N6	143.81(9)	156.30(5)	159.09(6)	155.54(8)	150.8(2)	154.65(7)	153.58(4)	151.02(4)
N5−M1−N6	72.41(9)	78.03(5)	79.47(6)	77.45(8)	75.4(2)	77.18(7)	77.22(4)	75.61(4)

Table 3. Averaged Bond Distances (Å) in $[ML_2]^{n+}$ Cations

	$C_{imine}-N_{imine}$	$C_{Py}-C_{imine}$	$N_{Py}-C_{Py}$
$[Mn^{II}L^0_2]^{2+}$	1.283(2)	1.498(2)	1.338(2)
$[Mn^{III}L^1_2]^+$	1.321(1)	1.442(1)	1.373(1)
$[Fe^{II}L^0_2]^{2+}$	1.309(1)	1.467(1)	1.353(1)
$[Co^{II}L^0_2]^{2+}$	1.295(2)	1.480(2)	1.349(2)
$[Co^{I}L^0_2]^+$	1.303(4)	1.465(4)	1.357(4)
$[Ni^{II}L^0_2]^{2+}$	1.290(2)	1.492(2)	1.341(2)
$[Cu^{II}L^0_2]^{2+}$	1.286(1)	1.496(1)	1.343(1)
$[Zn^{II}L^0_2]^{2+}$	1.285(1)	1.502(1)	1.336(1)

Scheme 3. Average $C_{imine}-N_{imine}$, $C_{imine}-C_{py}$, and $C_{py}-N_{py}$ Bond Lengths in $[Mn^{II}L^0_2](PF_6)_2$ (Left) and $[Mn^{III}L^1_2]PF_6$ (Right)

$[Mn^{II}L^0_2]^{2+}$ $[Mn^{III}L^1_2]^+$

(d^{10}) and a high-spin Mn^{II} (d^5) ion, respectively, four nearly equidistant $M-N_{imine}$ bonds and two relatively shorter $M-N_{py}$ bond distances are observed. This compression of the $N_{py}-M-N_{py}$ axis is observed in all structures.
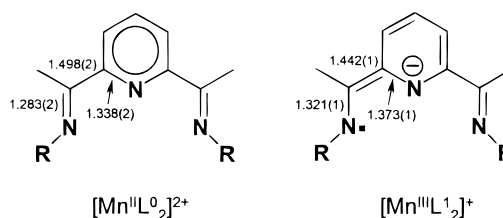
Although the Fe−N bond lengths in $[Fe^{II}L^0_2](PF_6)_2$ appear to be rather short (av Fe−N_{py} 1.868(1) Å; av Fe−N_{imine} 1.987-(1) Å), they compare well with those reported for low-spin $[Fe^{II}$-$(terpy)_2]^{2+}$ (av Fe−$N_{py-central}$ 1.891(4) Å; av Fe−$N_{py-distal}$ 1.988(3) Å).[26]

In $[Co^{II}L^0_2](PF_6)_2$ there are two longer Co−N_{imine} bonds at

~2.15 Å and two shorter ones at ~2.01 Å; the $Co-N_{py}$ bonds are not equivalent but are still the shortest at 1.852(2) and 1.991-(2) Å. This highly irregular CoN_6 polyhedron results from Jahn–Teller distortions of a low-spin Co^{II} ion (d^7) with an unsymmetrical occupancy of the e_g orbitals. Similar structures have been reported for low-spin Co^{II} complexes containing a macrocyclic bis(pyridine-2,6-diimine) ligand[27] or two terpyridine ligands.[28] Very similar Jahn–Teller distortions are also observed for the copper(II) complex (d^9) $[Cu^{II}L^0{}_2](PF_6)_2$.

In $[Co^IL^0{}_2]PF_6$, the one-electron-reduced form of $[Co^IL^0{}_2]$-$(PF_6)_2$, the $t_{2g}{}^6e_g{}^2$ electron configuration of the central Co^I ion yields again four equivalent $Co-N_{imine}$ bond lengths at ~2.14 Å and two equivalent $Co-N_{py}$ bonds at 1.99 Å. Crystallographically characterized Co^I (d^8) octahedral complexes ($S = 1$) with a CoN_6 octahedron are extremely rare. $[Co^I(bpy)_3]Cl \cdot H_2O$ is an example[29] where the average $Co-N$ distance has been determined to be 2.115(20) Å, in excellent agreement with the present structure where the average $Co-N$ distance is 2.093-(2) Å (in $[Co^{II}L^0{}_2](PF_6)_2$ this average $Co-N$ length is shorter at 2.031(2) Å). Similar results have been reported for the cobalt-(I) complex $[Co^I(L^{py})_2]^+$ containing two neutral tripodal ligands tris(2-pyridyl)methane (L^{py}).[30] The same is true for isoelectronic $[Ni^{II}L^0{}_2](PF_6)_2$.

The most remarkable structural changes are observed when the high-spin $[Mn^{II}L^0{}_2](PF_6)_2$ species is one-electron-reduced to the $[MnL_2]PF_6$ species. If one concurs with the notion from above that effectively both L^0 ligands are reduced to the radical anion $(L^1)^{1-}$, then the central Mn ion must have an oxidation state of $+III$. Since $[MnL_2]PF_6$ possesses an $S = 0$ ground state, it must then be a low-spin Mn^{III} ion ($S = 1$) that is strongly antiferromagnetically coupled to the two radical anions: $[Mn^{III}L^1{}_2]$-PF_6. In comparison to the MnN_6 octahedron in $[Mn^{II}L^0{}_2](PF_6)_2$ the corresponding polyhedron in $[Mn^{III}L^1{}_2]PF_6$ has $Mn-N$ distances that are on average 0.29 Å (!) *shorter*. This is a clear indication that whatever the true oxidation state of the central Mn ion is, namely, Mn^I (d^6), Mn^{II} (d^5), or Mn^{III} (d^4), it must possess a low-spin configuration with an empty $e_g{}^*$ orbital subset. In $[Mn^I(dapa)Br(CO)_2]$[16] the $Mn-N_{py}$ bond length is 1.944(4) Å and the two $Mn-N_{imine}$ distances are at 2.004(4) and 1.988(4) Å. (As noted above, the dapa ligand corresponds to an oxidation level of L^0.) The average $Mn-N_{py}$ and $Mn-N_{imine}$ bond lengths in $[MnL_2]PF_6$ at 1.885(1) and 1.984(1) Å are significantly shorter by 0.059 and 0.012 Å, respectively. Therefore, $[Mn^IL^0{}_2]PF_6$ can safely be ruled out.

Figure S3 shows a histogram where we have plotted all $Mn-N_{py}$ distances found in the Cambridge Crystallographic Structural Database. A total of 1106 complexes have been found containing the Mn–pyridine entity. The two maxima of $Mn-N_{py}$ bond lengths at ~2.28 and ~2.07 Å correspond to high-spin $Mn^{II}N_{py}$ and high-spin $Mn^{III}N_{py}$ (or $Mn^{IV}N_{py}$). The $Mn-N_{py}$ distance of 1.885(1) Å in $[MnL_2]PF_6$ is the shortest bond of this type reported to date. On the other hand, we have previously reported the crystal structure of a genuine low-spin

(26) Baker, A. T.; Goodwin, H. A. *Aust. J. Chem.* **1985**, *38*, 207.

(27) Drew, M. G. B.; McCann, M.; Nelson, S. M. *Inorg. Chim. Acta* **1980**, *41*, 213.

(28) (a) Figgis, B. N.; Kucharski, E. S.; White, A. H. *Aust. J. Chem.* **1983**, *36*, 1527. (b) Figgis, B. N.; Kucharski, E. S.; White, A. H. *Aust. J. Chem.* **1978**, *31*, 737.

(29) Szalda, D. J.; Creutz, C.; Mahajan, D.; Sutin, N. *Inorg. Chem.* **1983**, *22*, 2372.

(30) (a) Adam, K. R.; Anderson, P. A.; Astley, T.; Atkinson, I. M.; Charnock, J. M.; Garner, C. D.; Gulbis, J. M.; Hambley, T. W.; Hitchman, M. A.; Keene, F. R.; Tiekink, E. R. T. *J. Chem. Soc., Dalton Trans.* **1997**, 519. (b) Hafeli, T. A.; Keene, F. R. *Austr. J. Chem.* **1988**, *41*, 1379.

Table 4. Electrochemical Half-Wave Potentials[a]

	$[ML_2]^{3+}/[ML_2]^{2+}$	$[ML_2]^{2+}/[ML_2]^+$	$[ML_2]^+/[ML_2]^0$
$[ZnL^0{}_2]^{2+}$		-1.39	-1.67
$[FeL^0{}_2]^{2+}$	$+0.86$	-1.31	-1.66
$[CoL^0{}_2]^{2+}$	$+0.01$	-0.93	-1.92
$[NiL^0{}_2]^{2+}$ [b]	$+1.19$	-1.30	-1.82
$[CuL^0{}_2]^{2+}$	$+1.20^c$	-0.57	-1.21^c
$[MnL^0{}_2]^{2+}$	$+0.97$	$E_{anodic}: -1.21$	-1.87
		$E_{cathodic}: -0.62$	

[a] $E_{1/2}$ in volts vs Fc^+/Fc (CH_3CN (0.1 M [N(n-Bu)$_4$]PF$_6$); scan rate, 200 mV/s). [b] CH_2Cl_2 (0.1 M [N(n-Bu)$_4$]PF$_6$; 200 mV/s). [c] Irreversible; peak potentials $E_p{}^{ox}$, $E_p{}^{red}$ are given.

Mn^{II} complex ($S = {}^1/_2$) containing an MnN_6 octahedron.[31] The nitrogens are imine-type donors, and the polyhedron around the metal ion was described as a Jahn–Teller compressed octahedron with two short $Mn-N$ distances at 1.89(1) Å in trans position with respect to each other and four longer equatorial $Mn-N_{imine}$ bonds at an average of 1.985 Å. These values correspond exactly to those in $[MnL_2]PF_6$, and therefore, the description as a low-spin Mn^{II} coupling antiferromagnetically to one ligand radical $(L^1)^{1-}$ as in $[Mn^{II}L^0L^1]PF_6$ is a possibility, taking into consideration only the MnN_6 polyhedron. It would require the two ligands to be distinctly different, which they are not (see above). Thus, we favor the description as low-spin $[Mn^{III}L^1{}_2]PF_6$, which appears to accommodate the observed structural features of both the MnN_6 octahedron and the dimensions of the ligands $(L^1)^{1-}$. The $C_{imine}-N_{imine}$ *and* $N_{py}-C_{py}$ distances in the monocation $[MnL_2]^+$ are consistently $0.03-0.04$ Å longer than in the dication $[Mn^{II}L^0{}_2]^{2+}$, and the $C_{py}-C_{imine}$ distances are ~0.06 Å *shorter*. All other $C-C$ and $C-N$ distances are unaffected on going from $[MnL_2]^{2+}$ to $[MnL_2]^+$. We also note that all corresponding $C-C$ and $C-N$ bond distances in $[ZnL^0{}_2]^{2+}$ and $[Mn^{II}L^0{}_2]^{2+}$ are, within experimental error, the same as those in the uncoordinated, free L^0 ligand.[22] Thus, one-electron reduction of L^0 to $(L^1)^{1-}$ induces exactly the structural changes one expects, considering the resonance structures shown in Scheme 1.

Electro- and Spectroelectrochemical Investigations

Cyclic voltammograms (CV) of all complexes have been recorded in CH_3CN or CH_2Cl_2 solutions containing 0.10 M [N(n-Bu)$_4$]PF$_6$ as supporting electrolyte at a glassy carbon working electrode and a Ag/AgNO$_3$ reference electrode. Ferrocene was used as an internal standard, and potentials are referenced versus the ferrocenium/ferrocene couple (Fc^+/Fc). Table 4 summarizes the results.

Figure 4 (top) shows the CV of $[ZnL^0{}_2](PF_6)$ in the potential range $+1.3$ to -2.2 V. Two reversible one-electron-transfer waves are observed at quite negative potentials. Coulometric measurements establish that both processes correspond to a one-electron reduction that must be ligand-centered as depicted in eq 1.

$$[Zn^{II}L^0{}_2]^{2+} \underset{+e}{\overset{-e}{\rightleftharpoons}} [Zn^{II}L^0L^1]^+ \underset{+e}{\overset{-e}{\rightleftharpoons}} [Zn^{II}L^1{}_2]^0 \qquad (1)$$
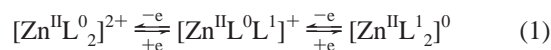
Thus, electrochemistry establishes that the coordinated L^0 ligand can be reduced to its monoanionic radical $(L^1)^{1-}$. Since both reduced forms are stable on the time scale of a coulometric experiment, we have recorded their electronic spectra, shown in Figure 5. We have also recorded the X-band EPR spectrum of $[Zn^{II}L^0L^1]^+$, which displays a featureless isotropic signal at

(31) Knof, U.; Weyhermüller, T.; Wolter, T.; Wieghardt, K. *J. Chem. Soc., Chem. Commun.* **1993**, 726.

Figure 4. Cyclic voltammograms of $[ZnL_2]PF_6$ (CH_3CN), $[FeL_2](PF_6)_2$ (CH_2Cl_2), $[CoL_2](PF_6)_2$ (CH_3CN), and $[NiL_2](PF_6)_2$ (CH_2Cl_2). Conditions are the following: 0.10 M $[N(n\text{-}Bu)_4]PF_6$ supporting electrolyte; glassy carbon working electrode; scan rate, 200 mV s^{-1}; 22 °C.
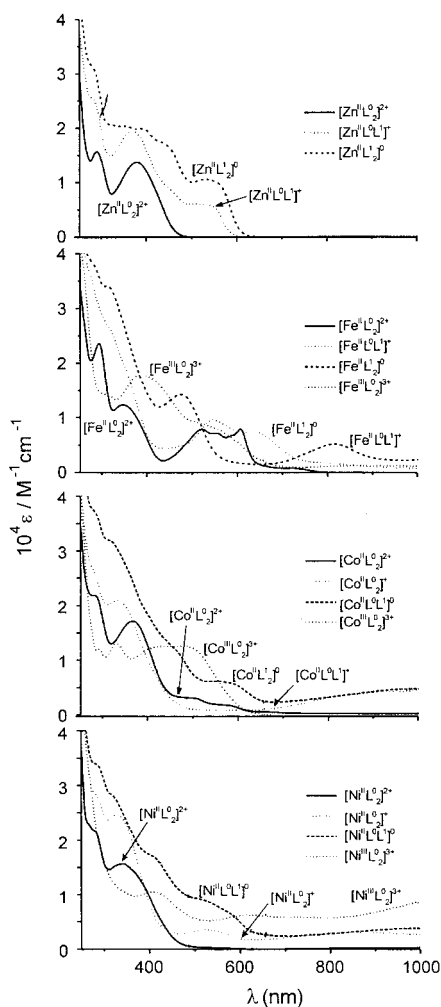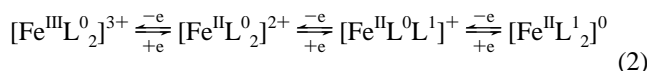

Figure 5. Electronic spectra of electrochemically generated $[ML_2]^{3+}$, $[ML_2]^+$, and $[ML_2]^0$ species. The spectra of $[ML_2]^{2+}$ complexes were recorded from acetonitrile solutions of the corresponding hexafluorophosphate salts. From top to bottom, M = Zn, Fe, Co, and Ni, respectively.

$g = 2.0008$ at 298 K without resolved hyperfine splitting and a sharp isotropic signal at $g = 2.0045$ at 10 K in frozen CH_3-CN solution, typical of an organic radical ($S = \frac{1}{2}$). The observed UV/vis spectral changes upon two successive one-electron reductions of $[Zn^{II}L^0_2]^{2+}$ are accompanied by the generation of a new charge transfer (CT) band of presumably $\pi-\pi^*$ character in the visible region (500–600 nm). Upon formation of $[Zn^{II}L^1_2]^0$ this band doubles in intensity and is a little red-shifted. The small difference between the two redox potentials of 280

mV is predominantly due to differences of solvation energies for a di- and monocationic pair and the monocation/neutral pair. Thus, the mixed-valent form $[Zn^{II}L^0L^1]^+$ does not experience a significant electronic stabilization via delocalization of the excess electron over two ligands. Consequently, in agreement with the additivity of the band in the visible region for $[Zn^{II}L^0L^1]^+$ and $[Zn^{II}L^1_2]^0$, we suggest that L^0 and $(L^1)^{1-}$ in $[ZnL^0L^1]^+$ have localized oxidation levels.

Figure 4 shows the CV of $[Fe^{II}L^0_2](PF_6)_2$. Three reversible one-electron waves are observed. Controlled potential coulometry at appropriately fixed potentials reveals that the process at $E_{1/2} = +0.86$ V corresponds to a one-electron oxidation that must be metal-centered, whereas the waves at $E_{1/2} = -1.31$ and -1.66 V correspond to ligand-centered successive one-electron reductions:

$$[Fe^{III}L^0_2]^{3+} \underset{+e}{\overset{-e}{\rightleftharpoons}} [Fe^{II}L^0_2]^{2+} \underset{+e}{\overset{-e}{\rightleftharpoons}} [Fe^{II}L^0L^1]^+ \underset{+e}{\overset{-e}{\rightleftharpoons}} [Fe^{II}L^1_2]^0 \quad (2)$$

The latter potentials are very similar to those observed for $[Zn^{II}L^0_2]^{2+}$, and the same arguments concerning the nature of $[Fe^{II}L^0L^1]^+$ apply. Since the oxidized[32] and two reduced forms of $[Fe^{II}L^0_2]^{2+}$ are stable at -20 °C on the time scale of coulometric experiments, we have recorded their electronic spectra, which are displayed in Figure 5. In general, the electro- and spectroelectrochemistry of $[Fe^{II}L^0_2]^{2+}$ is very similar to that reported by Toma et al.[14,15] for bis(2,6-diacetylfurfuryliminepyridine)iron(II) complexes, a notable exception being the spectrum of $[Fe^{II}L^1_2]^0$, which is clearly different from the analoguous species in Toma's work. The spectrum of $[Fe^{II}L^0_2]^{2+}$ is interesting with respect to that of $[ZnL^0_2]^{2+}$, since it displays a series of intense metal-to-ligand charge-transfer (MLCT) bands in the range 500–650 nm that are absent in the spectrum of $[ZnL^0_2]^{2+}$. These MLCT transitions are characteristic of iron-(II) diimine complexes.[14,15]

Since $[Fe^{II}L^0L^1]^+$ is stable in CH_3CN solution at -20 °C, we have recorded its X-band EPR spectrum shown in Figure S4. The slightly rhombic, almost isotropic signal could be satisfactorily simulated with the parameters $g_x = 1.996$, $g_y = 1.975$, $g_z = 1.961$ ($g_{av} = 1.977$). Evidently, the spectrum indicates formation of $[Fe^{II}L^0L^1]^+$ containing the ligand radical $(L^1)^{1-}$. Anion radical complexes of transition metal fragments usually display rather small deviations of g_e ($\Delta g \leq \pm 0.02$) because the spin is delocalized mainly over light atoms with small spin–orbit coupling factors.[33] The low g values of $[Fe^{II}L^0L^1]^+$ may be taken as a strong indication of at least one excited state close to the MLCT excited state of the nonreduced precursor complex $[Fe^{II}L^0_2]^{2+}$.[33]

The CV of $[Co^{II}L^0_2](PF_6)_2$ also displays three reversible one-electron-transfer waves (Figure 4). Coulometry established that at $E_{1/2} = 0.01$ V this species undergoes a one-electron oxidation that must be metal-centered, whereas the processes at -0.93 and -1.92 V correspond to two successive one-electron reductions. Note that the first reduction, $[CoL_2]^{2+}$ to $[CoL_2]^+$, occurs at a less negative potential than the ligand-centered, corresponding reductions in $[Zn^{II}L^0_2]^{2+}$ and $[Fe^{II}L^0_2]^{2+}$. There-

(32) The zero-field Mössbauer spectrum of electrochemically generated $[Fe^{III}L^0_2]^{3+}$ in frozen CH_3CN at 200 K shows a dominant quadrupole doublet (68%) for low-spin Fe(III) with $\delta = 0.056$ and $\Delta E_Q = 3.105$ mm s^{-1}, very similar to the values reported for $[Fe^{III}(terpy)_2]^{3+}$ ($\delta = 0.07$, $\Delta E_Q = 3.43$ mm s^{-1}; ref 24). However, a minor quadrupole doublet (32%) from a side product was also observed, indicative of high-spin Fe(III) with $\delta = 0.447$ and $\Delta E_Q = 0.718$ mm s^{-1}.

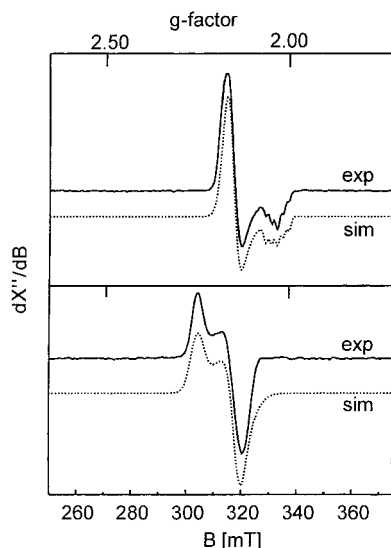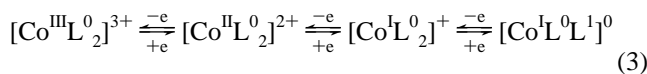(33) (a) Kaim, W. *Coord. Chem. Rev.* **1987**, *76*, 187. (b) Kaim, W. *Inorg. Chem.* **1984**, *23*, 3365.

Figure 6. X-band EPR spectra of electrochemically generated [Ni^{III}L$^0_2$]$^{3+}$ (top) and [Ni^{I}L$^0_2$]$^+$ (bottom) in frozen CH$_2$Cl$_2$ at 10 K. For [Ni^{III}L$^0_2$]$^{3+}$, conditions are the following: frequency, 9.4386 GHz; microwave power, 200.7 nW; modulation amplitude, 1.25 mT. For [Ni^{I}L$^0_2$]$^+$, conditions are the following: frequency, 9.4343 GHz; microwave power, 200.7 nW; modulation amplitude, 1.25 mT. The simulations were obtained using parameters given in the text.
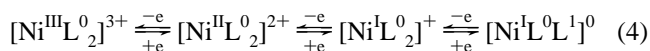
fore, and in agreement with the crystal structure, we assign this process to a metal-centered reduction Co^{II} → Co^I as in

$$[Co^{III}L^0_2]^{3+} \underset{+e}{\overset{-e}{\rightleftharpoons}} [Co^{II}L^0_2]^{2+} \underset{+e}{\overset{-e}{\rightleftharpoons}} [Co^IL^0_2]^+ \underset{+e}{\overset{-e}{\rightleftharpoons}} [Co^IL^0L^1]^0 \tag{3}$$

The electronic spectra of [Co^{III}L$^0_2$]$^{3+}$, [Co^{II}L$^0_2$]$^{2+}$, [Co$^IL^0_2$]$^+$, and [Co$^IL^0L^1$]^0 have been recorded and are shown in Figure 5.

The spectra of [Co$^IL^0_2$]$^+$ and [Co$^IL^0L^1$]^0 both exhibit an intense absorption at ~1000 nm with identical intensity. This transition is absent in the spectra of [Co^{III}L^0]$^{3+}$ and [Co^{II}L$^0_2$]$^{2+}$, and therefore, we assign it to a d−π^* MLCT band involving Co^I.[30] In addition, the spectrum of [Co$^IL^0L^1$]^0 displays an intense CT band in the range 500−600 nm, which indicates the presence of the radical (L^1)$^{1-}$. The intense broad band at 400−550 nm in the spectrum of [Co^{III}L$^0_2$]$^{3+}$ may be assigned to a LMCT band due to presence of Co^{III} (low-spin d^6). Note the similarity of this transition to that of isoelectronic [Fe^{II}L$^0_2$]$^{2+}$.

The CV of [Ni^{II}L$^0_2$](PF$_6$)$_2$ in CH$_2$Cl$_2$ (0.10 M [N(n-Bu)$_4$]PF$_6$) displays three reversible one-electron-transfer processes at $E_{1/2}$ = +1.19, −1.30, −1.82 V (Figure 4) of which the first has been established by controlled potential coulometry to be a one-electron oxidation whereas the last two correspond to two successive one-electron reductions. In conjunction with the EPR spectrum of [Ni$^IL^0_2$]$^+$ we assign these processes as in eq 4.

$$[Ni^{III}L^0_2]^{3+} \underset{+e}{\overset{-e}{\rightleftharpoons}} [Ni^{II}L^0_2]^{2+} \underset{+e}{\overset{-e}{\rightleftharpoons}} [Ni^IL^0_2]^+ \underset{+e}{\overset{-e}{\rightleftharpoons}} [Ni^IL^0L^1]^0 \tag{4}$$

The electronic spectra of [NiL$_2$]$^{n+}$ (n = 3, 2, 1, 0) are shown in Figure 5 (bottom).

We have recorded the X-band EPR spectra of electrochemically generated [Ni^{III}L$^0_2$]$^{3+}$ and [Ni$^IL^0_2$]$^+$ in frozen CH$_2$Cl$_2$ solutions at 10 K. These are shown in Figure 6. The EPR spectrum of [Ni^{III}L$^0_2$]$^{3+}$ (Figure 6, top) shows an axial signal with $g_\parallel < g_\perp$, of which $g_\parallel$ is split into a well resolved quintet as a result of hyperfine coupling with two equivalent nitrogen
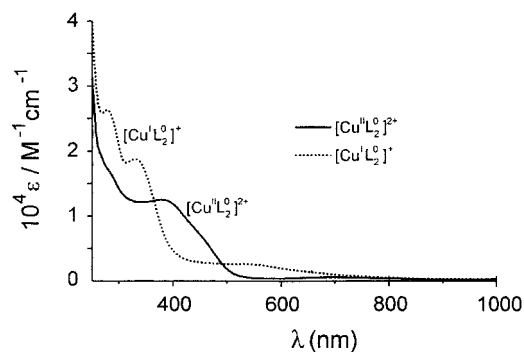

Figure 7. Electronic spectra of [Cu^{II}L$^0_2$](PF$_6$)$_2$ and electrochemically generated [Cu$^IL^0_2$]$^+$ in CH$_2$Cl$_2$ solution.

nuclei ($I = 1$). Simulation reveals the following parameters: $g_\perp = 2.129$, $g_\parallel = 2.022$, $A^N_\parallel = 60 \times 10^{-4}$ cm^{-1}, $A_\perp =$ unresolved.

Interestingly, the EPR spectrum of [Ni$^IL^0_2$]$^+$ (Figure 6, bottom) also shows an axial spectrum but with $g_\parallel > g_\perp$. No resolved hyperfine couplings were observed. The simulation gives $g_\parallel = 2.213$, $g_\perp = 2.115$.

Remarkably, the situation $g_\parallel < g_\perp$ holds for both the (isoelectronic) low-spin d^7 species [Ni^{III}L$^0_2$]$^{3+}$ and [Co^{II}L$^0_2$]$^{2+}$, whereas $g_\parallel > g_\perp$ is observed for each of the d^9 species [Ni$^IL^0_2$]$^+$ and [Cu^{II}L$^0_2$]$^{2+}$ (vide supra).

We define the N−M−N axis with the longest M−N distances as the molecular z axis (Table 2). Thus, the d$_{z^2}$ orbital points in the direction of two N$_{imine}$ donors in both [Co^{II}L$^0_2$]$^{2+}$ (half-filled d$_{z^2}$) and [Cu^{II}L$^0_2$]$^{2+}$ (filled d$_{z^2}$, half filled d$_{x^2-y^2}$), as derived from the observed Jahn−Teller distortions in the X-ray structures. In good agreement, $g_\parallel < g_\perp$ indicates an unpaired electron in d$_{z^2}$ for [Ni^{III}L$^0_2$]$^{3+}$ and [Co^{II}L$^0_2$]$^{2+}$, whereas $g_\parallel > g_\perp$ suggests an unpaired electron in d$_{x^2-y^2}$ for [Ni$^IL^0_2$]$^+$ and [Cu^{II}L$^0_2$]$^{2+}$.[34] The observed hyperfine coupling with *two* equivalent N nuclei of $g_\parallel$ in the spectrum of [Ni^{III}L$^0_2$]$^{3+}$ supports our idea that the unpaired electron is localized in the d$_{z^2}$ orbital.

The CV of [Cu^{II}L$^0_2$](PF$_6$)$_2$ displays one fully reversible one-electron-transfer wave at $E_{1/2} = -0.57$ V in the potential range +1.4 to −2.2 V. An irreversible oxidation occurs at $E_p^{ox} = +1.20$ V, and a further irreversible reduction is observed at −1.21 V. Both processes were not further investigated. The one-electron reduction is most likely metal-centered, as is deduced from the electronic spectrum shown in Figure 7 of the reduced form, which does not display the radical bands of (L^1)$^{1-}$.

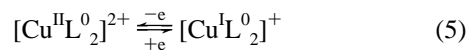$$[Cu^{II}L^0_2]^{2+} \underset{+e}{\overset{-e}{\rightleftharpoons}} [Cu^IL^0_2]^+ \tag{5}$$

Figure 8 shows the remarkable CV of [Mn^{II}L$^0_2$](PF$_6$)$_2$ in CH$_2$Cl$_2$, which is the same in CH$_3$CN (0.10 M [N(n-Bu)$_4$]PF$_6$). It displays at a very positive potential, $E_{1/2}^{ox} = +0.97$ V, and at a very negative potential, $E_{1/2}^{red2} = -1.87$ V, two fully reversible one-electron-transfer waves, but—in between—at medium potential an apparently irreversible couple of a reduction ($E_p^{red} = -1.21$ V) and an oxidation wave ($E_p^{ox} = -0.62$ V) are observed. At a scan rate of 200 mV s^{-1} the two processes are separated by 0.59 V (!). Amazingly, this CV does not change upon repetitive scanning, which indicates that both "irreversible" processes do not lead to chemical decomposition of the complex. The CV of [Mn^{III}L$^1_2$]PF$_6$ is almost identical except that in the first cycle the reduction wave at −1.21 V is not observed when the scan is started between the couple even after allowing for

(34) Goodman, B. A.; Raynor, J. B. *Adv. Inorg. Chem. Radiochem.* **1970**, *13*, 135−361.
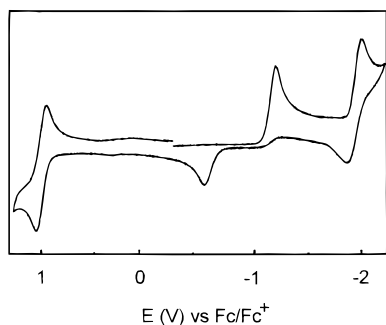
Figure 8. Cyclic voltammogram of $[Mn^{II}L^0_2](PF_6)_2$ in CH_3CN (0.10 M [N(n-bu)$_4$]PF$_6$) at a glassy carbon electrode; scan rate, 200 mV s^{-1}.

an equilibration period of 15 s at the starting potential. In the second and all following cycles after having passed through the oxidation wave at -0.62 V the missing peak appears at the same potential as observed for $[Mn^{II}L^0_2](PF_6)_2$. This is good evidence that the two separated peaks, E^{ox} and E^{red}, correspond to the chemically reversible interconversion of $[Mn^{II}L^0_2]^{2+}$ and $[Mn^{III}L^1_2]^+$, as is supported by the spectroelectrochemical investigations (see below).

There are two mechanistically different origins conceivable for this behavior of the couple $[Mn^{II}L^0_2]^{2+}/[Mn^{III}L^1_2]^+$: (i) slow electrode kinetics due to a substantial reorganization energy (large Franck–Condon barrier) of the reduced or oxidized complex; (ii) the involvement of two reaction intermediates on going from $[Mn^{II}L^0_2]^{2+}$ to $[Mn^{III}L^1_2]^+$ and vice versa.[35] Both mechanisms differ in their response to the scan rate; a 10-fold increase of the scan rate gives rise to an increase in peak separation, $|E_p^{ox} - E_p^{red}|$, of 120 mV, if mechanism i is operative, whereas a homogeneous first-order followup reaction gives rise to a peak separation of only 60 mV per 10-fold increase of the scan rate. As shown in Figure 9, a 10-fold increase in scan rate shifts the peak position E_p^{red} by 31 mV toward more negative potentials whereas E_p^{ox} is shifted by 33 mV to more positive potentials. The resulting increase in peak separation of 64 mV strongly supports a mechanism invoking two short-lived intermediates (EC–EC mechanism).

We have also performed CV experiments of $[Mn^{II}L^0_2]^{2+}$ at scan rates up to 5×10^4 V s^{-1} in a 10 μm diameter ultramicroelectrode cell. The two well-separated peaks E_p^{red} and E_p^{ox} are still observed at these very fast scan rates. This clearly demonstrates that both putative intermediates must have lifetimes shorter than 10^{-5} s; i.e., their forward rate constants of decay, k_f, is $>10^5$ s^{-1}. Otherwise, reversible one-electron-transfer waves at $E_{1/2} \approx -1.5$ V (starting the scan at 0.0 V) or at about -0.5 V (starting at -1.7 V) would have been observed. Along the same lines, the back reactions must be slow ($k_b < 0.1$ s^{-1}), because otherwise, reversible one-electron-transfer peaks would have been observed at slow scan rates.

Scheme 4 gives a mechanistic proposal invoking an EC–EC mechanism that accommodates the electrochemical results. We suggest a cycle where the high-spin complex $[Mn^{II}L^0_2]^{2+}$ (starting material) accepts an electron into one of the L^0 ligands forming intermediate **1**, $[Mn^{II}L^0L^1]^+$, which rapidly rearranges intramolecularly to the product $[Mn^{III}L^1_2]^+$. Upon one-electron oxidation of this form the second intermediate, **2**, namely, $[Mn^{III}L^0L^1]^{2+}$, is formed, which again rapidly isomerizes intramolecularly to the product $[Mn^{II}L^0_2]^{2+}$. The two back reactions $[Mn^{III}L^1_2]^+ \rightarrow [Mn^{II}L^0L^1]^+$ (intermediate **1**) and $[Mn^{II}L^0_2]^{2+} \rightarrow [Mn^{III}L^0L^1]^{2+}$ (intermediate **2**) are slow.

(35) Bard, A. J.; Faulkner, L. R. *Electrochemical Methods, Fundamentals and Applications*; John Wiley & Sons: New York, 1980; Chapters 6 and 11 and references therein.
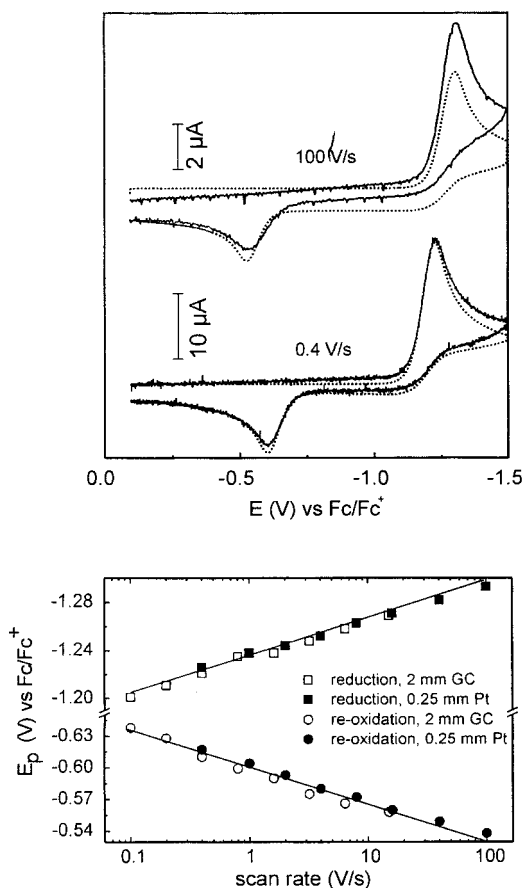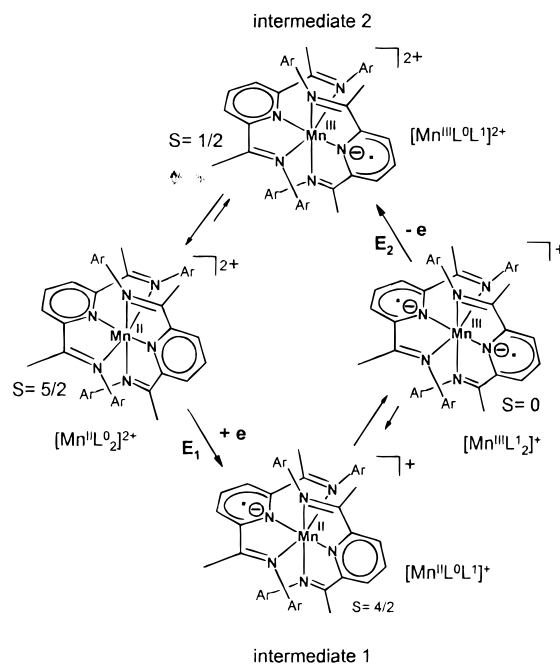

Figure 9. Top: cyclic voltammograms of $[Mn^{II}L^0_2]^{2+}$ at two different scan rates and their simulations (Scheme 4). Parameters are given in the text. Bottom: dependence of peak separation $E_p^{ox} - E_p^{red}$ on the scan rate.

Scheme 4. Mechanistic Proposal for an EC–EC Mechanism for the Reversible Interconversion $[Mn^{III}L^1_2]^+ \rightleftharpoons [Mn^{II}L^0_2]^{2+} + e$


This EC–EC mechanistic scheme in conjunction with the above limits for the rate constants k_f and k_b allows one to satisfactorily simulate the CV's at all scan rates of the

interconversion $[Mn^{II}L^0_2]^{2+} + e^- \rightleftharpoons [Mn^{III}L^1_2]^+$. Examples of two scan rates are shown in Figure 9.

Since the actual peak positions E_p^{ox}, E_p^{red} in a given cyclic voltammetric experiment are governed independently from each other by the intrinsic redox potentials E_1 and E_2 for the two couples $[Mn^{II}L^0_2]^{2+}/[Mn^{II}L^0L^1]^+$ and $[Mn^{III}L^0L^1]^{2+}/[Mn^{III}L^1_2]^+$ and by the rates of the intramolecular followup reactions, k_f and k_f', there is not only one set of parameters that gives a satisfactory fit to the available experimental data. Thus, a change in the reaction rates by a factor of 10 has the same effect as a shift in E_1 or E_2 by 30 mV. Since the rate constants k_f and k_f' are in the range 10^5-10^{13} s^{-1}, the redox potential for the couple $[Mn^{II}L^0_2]^{2+}/[Mn^{II}L^0L^1]^+$ can be estimated to be in the range -1.31 to -1.55 V, and at the same time, the redox potential of the couple $[Mn^{III}L^0L^1]^{2+}/[Mn^{III}L^1_2]^+$ is in the range -0.52 to -0.28 V. All other parameters are of only minor importance for the peak positions E_p^{ox}, E_p^{red}. Interestingly, the estimated redox potential for the $[Mn^{II}L^0_2]^{2+}/[Mn^{II}L^0L^1]^+$ couple at -1.31 to -1.55 V is in the vicinity of the couples $[ZnL^0_2]^{2+}/[ZnL^0L^1]^+$ at -1.39 V and $[Fe^{II}L^0_2]^{2+}/[Fe^{II}L^0L^1]^+$ at -1.31 V. In all these cases an L^0 ligand coordinated to a divalent metal ion is reversibly reduced to a monoanionic ligand radical $(L^1)^{1-}$. We feel that this observation is strong evidence that the interpretation given in Scheme 4 is essentially correct.

The reversible one-electron oxidation at $E_{1/2} = +0.97$ V is proposed to be metal-centered,

$$[Mn^{II}L^0_2]^{2+} \rightleftharpoons [Mn^{III}L^0_2]^{3+} + e \qquad (6)$$
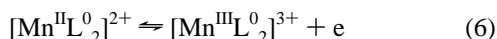
whereas the reversible one-electron transfer at very negative potentials, e.g., $E_{1/2} = -1.87$ V, may correspond to a metal-centered one-electron reduction of $[Mn^{III}L^1_2]^+$,

$$[Mn^{III}L^1_2]^+ + e^- \rightleftharpoons [Mn^{II}L^1_2]^0 \qquad (7)$$

The spectral changes observed upon coulometric one-electron reduction of $[Mn^{II}L^0_2]^{2+}$ to $[Mn^{III}L^1_2]^+$ at a fixed potential of -1.40 V and subsequent reoxidation at $+0.05$ V are shown in Figure S5. Both processes proceed smoothly; three well-defined isosbestic points are observed at 244, 387, and 499 nm. The final spectra of these electrochemically generated species are identical to those of CH$_3$CN solutions of solid materials $[Mn^{II}L^0_2](PF_6)_2$ and $[Mn^{III}L^1_2]PF_6$. The inset in Figure S5 shows the time dependence of the absorption maxima at 231 and 633 nm during electrolytic reduction and reoxidation. Thus, although the complicated waveform and the peak separation in the CV of $[Mn^{II}L^0_2]^{2+}$ apparently indicated otherwise, the $[Mn^{II}L^0_2]^{2+}/[Mn^{III}L^1_2]^+$ redox couple is fully reversible on the time scale of a coulometric experiment (40 s).

Figure 10 shows the spectra of electrochemically generated $[Mn^{III}L^0_2]^{3+}$, $[Mn^{II}L^0_2]^{2+}$, and $[Mn^{III}L^1_2]^+$ and of the fully reduced $[MnL_2]^0$ species. Upon reduction of $[Mn^{III}L^1_2]^+$ to $[Mn^{II}L^1_2]^0$ the characteristic MLCT bands at 633 and 815 nm disappear and a new band between 500 and 600 nm grows in. This band is similar to that of $[Zn^{II}L^1_2]^0$ (Figure 5) and indicates the presence of $(L^1)^{1-}$ ligands. Thus, this reduction is metal-centered $Mn^{III} \rightarrow Mn^{II}$ yielding $[Mn^{II}L^1_2]^0$.

Discussion

All characterized tricationic species $[ML_2]^{3+}$ contain two neutral L^0 ligands and a trivalent metal ion: M = Mn^{III} (d^4 low-spin (?), $S = 1$ (?)); M = Fe^{III} (d^5 low-spin, $S = \frac{1}{2}$); M = Co^{III} (d^6 low-spin, $S = 0$); M = Ni^{III} (d^7 low-spin, $S = \frac{1}{2}$) Similarly, all dications also contain two neutral L^0 ligands and

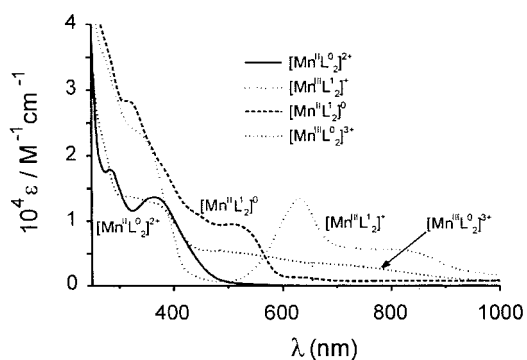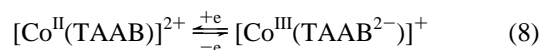**Figure 10.** Electronic spectra of electrochemically generated $[MnL_2]^{n+}$ (n = 3, 2, 1, 0) species (CH$_3$CN).

a central divalent metal ion: M = Mn^{II} (d^5 high-spin, $S = \frac{5}{2}$); M = Fe^{II} (d^6 low-spin, $S = 0$); M = Co^{II} (d^7 low-spin, $S = \frac{1}{2}$), M = Ni^{II} (d^8, $S = 1$); M = Zn^{II} (d^{10}, $S = 0$).

For the monocations $[ML_2]^+$ the situation is more diverse: the zinc complex due to the stability of a Zn^{II} (d^{10}) configuration contains one coordinated L^0 and one radical anion $(L^1)^{1-}$, $[Zn^{II}L^0L^1]^+$ $(S = \frac{1}{2})$, whereas $[MnL_2]^+$ is described as $[Mn^{III}L^1_2]^+$. However, we cannot directly discriminate between the following discriptions on the basis of the experimental data: (1) electrons unpaired—a low-spin manganese(III) ion $(S = 1)$ antiferromagnetically coupled to two ligand radicals $(L^1)^{1-}$ $(S = \frac{1}{2})$, yielding the observed singlet ground state $(S = 0)$; (2) electrons paired—a delocalized model in which all six electrons are paired but delocalized over the manganese t$_{2g}$ and ligand π^* orbitals (π-back-bonding model).

In principle, model 2 might be regarded as manganese(I) with strong π-back-bonding to the ligand π^* orbitals. However, to explain the experimental data, this interaction should be (nearly) covalent, leading to a net charge distribution in which each ligand π^* orbital is filled with one electron. As such, the description $[Mn^{III}L^1_2]^+$, and not $[Mn^{I}L^0_2]^+$, is still valid.

We are aware of only two precedents[36,37] in which (one-electron) reduction of a transition metal complex results in a net *increase* of the metal oxidation state through charge redistribution within the ligands, i.e., eqs 8 and 9 where TAAB represents a tetraaza[16]annulene macrocycle, Cl$_4$SQ is the tetrachlorosemiquinonate anion, and Cl$_4$Cat is the tetrachlorocatecholate dianion.

$$[Co^{II}(TAAB)]^{2+} \underset{-e}{\overset{+e}{\rightleftharpoons}} [Co^{III}(TAAB^{2-})]^+ \qquad (8)$$

and

$$[V^{III}(Cl_4SQ)_3]^0 \underset{-e}{\overset{+e}{\rightleftharpoons}} [V^V(Cl_4Cat)_3]^- \qquad (9)$$

$[FeL_2]^+$ $(S = \frac{1}{2})$ must be described as a low-spin ferrous species (d^6 low-spin; $S = 0$) containing one ligand radical $(L^1)^{1-}$ $(S = \frac{1}{2})$ and one L^0: $[Fe^{II}L^0L^1]^+$. In contrast, $[CoL_2]^+$ $(S = 1)$ contains a cobalt(I) ion (d^8, $S = 1$) and two L^0: $[Co^{I}L^0_2]^+$. Similarly, $[NiL_2]^+$ $(S = \frac{1}{2})$ contains a Ni^{I} (d^9, $S = \frac{1}{2}$) ion and two L^0: $[Ni^{I}L^0_2]^+$. $[CuL_2]^+$ $(S = 0)$ contains two L^0 ligands and a Cu^{I} (d^{10}, $S = 0$) ion. It is conceivable that the two L^0 ligands in this species are only bidentate, giving rise to a Cu^{I}N$_4$ polyhedron and two "dangling" uncoordinated imine nitrogens.

(36) Cass, M. E.; Gordon, N. R.; Pierpont, C. G. *Inorg. Chem.* **1986**, *25*, 3962.

(37) Takvoryan, N.; Faramery, K.; Katovic, V.; Lovecchio, F. V.; Gore, E. S.; Anderson, L. B.; Busch, D. H. *J. Am. Chem. Soc.* **1974**, *96*, 731.

Because of their extraordinarily strong reducing power, the neutral species $[ML_2]^0$ are the least well-characterized complexes of the series. None has been isolated as a crystalline solid. It is safe to assume that $[ZnL_2]$ actually is $[Zn^{II}L^1_2]^0$, but its electronic ground state is not known. $S = 0$ or $S = 1$ is possible if intramolecular anti- or ferromagnetic coupling of the two $(L^1)^{1-}$ radicals prevails. $[MnL_2]$ contains most likely two $(L^1)^{1-}$ ligands and a low-spin Mn^{II} ion, i.e., $[Mn^{II}L^1_2]$ ($S = 1/2$), and $[FeL_2]^0$ probaby contains a low-spin Fe^{II} ion and two $(L^1)^{1-}$, i.e., $[Fe^{II}L^1_2]^0$. $[CoL_2]^0$ is probaby $[Co^IL^0L^1]^0$, and $[NiL_2]^0$ is then $[Ni^IL^0L^1]$ on the basis of the argument that Co^0 and Ni^0 in an octahedral N_6 environment have not been observed in a coordination compound and that the $+I$ oxidation state of the two metal ions is accessible already in the dications.

In summary, we have shown that pyridine-2,6-diimine ligands are noninnocent.

Experimental Section

General Procedures. All reactions were performed under an argon atmosphere using standard Schlenk techniques unless indicated otherwise. Solvents (p.a.) were deoxygenated by passing a stream of argon through solutions or by the freeze−pump−thaw method. The ligand 2,6-bis[1-(4-methoxyphenylimino)ethyl]pyridine (L^0) was prepared as described previously.[5] All other chemicals are commercially available and were used without further purification.

Physical Measurements. Electronic spectra of the complexes and spectra of the spectroelectrochemical investigations were recorded on a HP 8452A diode array spectrophotometer (range: 221−1100 nm). Cyclic voltammograms, square-wave voltammograms and coulometric experiments were performed using an EG&G potentiostat/galvanostat. Simulations of the cyclic voltammograms were obtained using the program DigiSim 3.0. (Bioanalytical Systems, Inc., West Lafayette, IN). Temperature-dependent (2−298 K) magnetization data were recorded on a SQUID magnetometer (MPMS Quantum design) in an external magnetic field of 1.0 T. The experimental susceptibility data were corrected for underlying diamagnetism by the use of tabulated Pascal's constants.

IR spectra were recorded on a Perkin-Elmer FT-IR spectrometer 2000. X-band EPR spectra were recorded on a Bruker ESP 300. The spectra were simulated by iteration of the (an)isotropic g values, hyperfine coupling constants, and line widths. We thank Dr. F. Neese (Abteilung Biologie der Universität Konstanz) for a copy of his EPR simulation program. NMR experiments were carried out on a Bruker ARX250 (250 and 63 MHz for ^1H and ^{13}C NMR, respectively) and a Bruker WM400 (400 and 100 MHz for ^1H and ^{13}C NMR, respectively). Internal shift reference for ^1H NMR, with CHD_2CN, is $\delta_H = 1.94$. Internal shift reference for ^{13}C NMR, with CD_3CN, is $\delta_C = 118.3$. Abbreviations used are the following: s = singlet, d = doublet, t = triplet. Mössbauer data were recorded on an alternating constant-acceleration spectrometer. The minimum experimental line width was 0.24 mm s^{-1} (full width at half-height). A constant sample temperature was maintained with an Oxford Instruments Variox or an Oxford Instruments Mössbauer-Spectromag 2000 Cryostat. The latter is a split-pair superconducting magnet system for applied fields up to 8 T in which the sample temperature can be varied between 1.5 and 250 K with the field of the sample oriented perpendicular to the γ-beam. The $^{57}Co/Rh$ source (1.8 GBq) was positioned at room-temperature inside the gap of the magnet system at zero-field positions. Reported isomer shifts (δ) are referenced versus iron metal at 300 K.

X-ray Structure Determinations. Single crystals of orange-red $[Mn^{II}L^0_2](PF_6)_2$, deep-blue $[Mn^{III}L^1_2]PF_6$, purple-black $[Fe^{II}L^0_2](PF_6)_2$, brown-black $[Co^{II}L^0_2](PF_6)_2$, green-black $[Co^IL^0_2]PF_6$, brown $[Ni^{II}L^0_2](PF_6)_2$, brown $[Cu^{II}L^0_2](PF_6)_2$, and yellow $[Zn^{II}L^0_2](PF_6)_2$ were mounted in glass capillaries sealed under argon. Graphite monochromated Mo Kα radiation ($\lambda = 0.710\ 73$ Å) was used throughout. Final cell constants were obtained from a least-squares fit of a subset of several thousand strong reflections. Data collection was performed by hemisphere runs taking frames between 0.3° and 1.0° in ω. The CCD detector system diffractometers were equipped with a cryogenic nitrogen cold stream.

Intensity data were collected at 100(2) K. Semiempirical absorption corrections using the program SADABS[38] were performed on data sets collected with the SMART system. Crystallographic data of the compounds and diffractometer types used are listed in Table 5. The Siemens ShelXTL[39] software package was used for solution, refinement, and artwork of the structures. All structures were readily solved and refined by direct methods and difference Fourier techniques. All non-hydrogen atoms were refined anisotropically except the minor split component of a disordered PF_6-anion in $[Mn^{II}L^0_2](PF_6)_2$. A split atom model was used here with occupancies of 0.7 and 0.3. All hydrogen atoms bound to carbon were placed at calculated positions and refined as riding atoms with isotropic displacement parameters. The hydrogen atoms of a water molecule in $[Fe^{II}L^0_2](PF_6)_2 \cdot H_2O$ could not be located from the difference map and were therefore not included in the refinement.

Synthesis of Complexes. 1. $[Zn^{II}L^0_2](PF_6)_2$. Amounts of 0.30 g (1.01 mmol) of $Zn(NO_3)_2 \cdot 6H_2O$ and 0.33 g (0.88 mmol) of 2,6-bis[1-(4-methoxyphenylimino)ethyl]pyridine (L^0) were dissolved in 18 mL of MeOH, and the mixture was stirred at 20 °C for 30 min. Subsequently, 1.00 g (6.1 mmol) of NH_4PF_6 was added to the yellow solution, causing the precipitation of $[Zn^{II}L^0_2](PF_6)_2$ as yellow platelike crystals. The solid was collected by filtration, washed three times (10 mL) with ice-cold MeOH, air-dried, and recrystallized from CH_3CN/Et_2O. Yield: 436 mg (90% based on L^0 ligand) as yellow crystals. FT-IR (KBr, cm^{-1}): 1630, 1601, 1587 ($\nu(C=N)$ + aryl- and pyridyl-ring deformations), 841, 558 (PF_6^-). ESI-MS, m/z: 955 $[M - PF_6]^+$, 405 $[M - 2PF_6]^{2+}/2$. Anal. Calcd for $C_{46}H_{46}F_{12}N_6O_4P_2Zn$: C, 50.13; H, 4.21; N, 7.62; Zn, 5.93. Found: C, 50.00; H, 4.18; N, 7.69, Zn, 5.79.

2. $[Co^{II}L^0_2](PF_6)_2$. Amounts of 0.23 g (1.76 mmol) of $CoCl_2$ and 0.33 g (0.88 mmol) of 2,6-bis[1-(4-methoxyphenylimino)ethyl]pyridine (L^1) were dissolved in 25 mL of MeOH, and the mixture was stirred at 20 °C for 30 min. Subsequently, 1.00 g (6.1 mmol) of NH_4PF_6 was added to the dark-brown solution, causing the precipitation of $[Co^{II}L^0_2]$-$(PF_6)_2$ as a brown solid. The solid was collected by filtration, washed three times (10 mL) with ice-cold MeOH, air-dried, and recrystallized from CH_3CN/Et_2O. Yield: 455 mg (94% based on L^0 ligand) as brown-black crystals. FT-IR (KBr, cm^{-1}): 1603, 1582 ($\nu(C=N)$ + py- and aryl-ring deformations), 841, 558 (PF_6^-). ESI-MS, m/z: 950 $[M - PF_6]^+$, 402.5 $[M - 2PF_6]^{2+}/2$. Anal. Calcd for $C_{46}CoH_{46}F_{12}N_6O_4P_2$: C, 50.42; H, 4.23; N, 7.67; Co, 5.38. Found: C, 50.31; H, 4.18; N, 7.75, Co, 5.45.

3. $[Co^IL^0_2]PF_6$. Treatment of a brown solution of 200 mg (0.18 mmol) of $[Co^{II}L^0_2](PF_6)_2$ in 8 mL of CH_3CN with 52 mg (0.27 mmol) of cobaltocene resulted in a dark-green solution. This solution was stirred for 30 min and subsequently top-layered with Et_2O. After a few days, a mixture of dark-green/black crystals of $[Co^IL^0_2]PF_6$ and bright-yellow crystals $[Cp_2Co]PF_6$ were collected. The yellow $[Cp_2Co]PF_6$ material was removed by washing the mixture with hot water (50 °C) until the water came off colorless. Yield: 109 mg (64%) of $[Co^IL^0_2]$-PF_6 as green/black crystals. FT-IR (KBr, cm^{-1}): 1622, 1603, 1592, 1580 ($\nu(C=N)$ + py- and aryl-ring deformations), 841, 558 (PF_6^-). Anal. Calcd for $C_{46}CoH_{46}F_6N_6O_4P$: C, 58.11; H, 4.88; N, 8.84; Co, 6.20. Found: C, 57.80; H, 4.86; N, 8.65, Co, 5.47.

4. $[Mn^{II}L^0_2](PF_6)_2$. Amounts of 1.10 g (4.38 mmol) of $Mn(NO_3)_2 \cdot 4H_2O$ and 1.0 g (2.68 mmol) of 2,6-bis[1-(4-methoxyphenylimino)-ethyl]pyridine (L^0) were dissolved in 50 mL of MeOH, and the mixture was stirred at 20 °C for 30 min. Subsequently, 3.00 g (18.4 mmol) of NH_4PF_6 was added to the orange-red solution, causing the precipitation of $[Mn^{II}L^0_2](PF_6)_2$ as an orange microcrystalline solid. The solid was collected by filtration, washed three times (10 mL) with ice-cold MeOH, and air-dried. Yield: 1.40 g (96% based on L^0 ligand). FT-IR (KBr, cm^{-1}): 1624, 1603, 1584 ($\nu(C=N)$ + py- and aryl-ring deformations), 841, 558 (PF_6^-). ESI-MS, m/z: 946 $[M - PF_6]^+$. Anal. Calcd for $C_{46}H_{46}F_{12}MnN_6O_4P_2$: C, 50.61; H, 4.25; N, 7.70; Mn, 5.03. Found: C, 49.96; H, 3.79; N, 7.73, Mn, 4.50.

5. $[Mn^{III}L^1_2]PF_6$. Treatment of an orange-red solution of 504 mg (0.46 mmol) of $[Mn^{II}L^0_2](PF_6)_2$ in 10 mL of CH_3CN with 100 mg (0.53

(38) Sheldrick, G. M. Universität Göttingen, Germany, 1994.

(39) *ShelXTL*, version 5; Siemens Analytical X-ray Instruments, Inc.: Madison, WI, 1994.

Table 5. Crystallographic Data[a]

	[Mn^II L^0_2](PF_6)_2	[Mn^III L^1_2]PF_6	[Fe^II L^0_2](PF_6)_2·H_2O	[Co^II L^0_2](PF_6)_2	[Co^I L^0_2]PF_6	[Ni^II L^0_2](PF_6)_2	[Cu^II L^0_2](PF_6)_2	[Zn^II L^0_2](PF_6)_2
chemical formula	C_46H_46F_12MnN_6O_4P_2	C_46H_46F_6MnN_6O_4P	C_46H_48F_12FeN_6O_5P_2	C_46H_46CoF_12N_6O_4P_2	C_46H_46CoF_6N_6O_4P	C_46H_46F_12N_6NiO_4P_2	C_46H_48CuF_12N_6O_5P_2	C_46H_46F_12N_6O_4P_2Zn
fw	1091.77	946.80	1110.69	1095.76	950.79	1095.54	1100.37	1102.20
diffractometer	Siemens Smart	Nonius Kappa CCD	Nonius Kappa CCD	Siemens Smart	Nonius Kappa CCD	Siemens Smart	Nonius Kappa CCD	Nonius Kappa CCD
space group	$P2_1/c$	$P2_1/c$	$P2_1/c$	$P2_1/c$	$P\bar{1}$	$P2_1/c$	$P2_1/c$	$P2_1/c$
a, Å	19.973(4)	12.3162(8)	18.455(2)	18.104(2)	13.142(3)	18.047(2)	17.7990(8)	17.807(2)
b, Å	15.102(3)	23.911(3)	16.4501(12)	16.5602(14)	14.080(3)	16.655(2)	16.7966(8)	16.825(2)
c, Å	17.257(4)	14.6946(9)	17.224(2)	17.248(2)	14.7524(4)	17.132(2)	17.1107(8)	17.037(2)
α, deg	90	90	90	90	111.50(3)	90	90	90
β, deg	113.89(3)	93.96(2)	114.81(2)	113.83(2)	102.85(3)	112.70(2)	111.890(10)	111.38(2)
γ, deg	90	90	90	90	110.04(3)	90	90	90
V, Å^3	4759(2)	4317.2(5)	4746.4(8)	4730.2(9)	2188.7(8)	4750.5(10)	4746.6(4)	4753.1(10)
Z	4	4	4	4	2	4	4	4
temp, K	100(2)	100(2)	100(2)	100(2)	100(2)	100(2)	100(2)	100(2)
ρ calcd, g cm^-3	1.524	1.457	1.554	1.539	1.443	1.532	1.540	1.540
μ (Mo Kα), mm^-1	0.442	0.421	0.486	0.529	0.506	0.574	0.626	0.682
no. reflns	36 091	61 521	81 673	41 247	8827	32 080	97 330	33 840
unique reflns/ [I > 2σ(I)]	8275/6359	9876/7824	13 832/10052	10 763/7076	6076/3916	6841/5872	17 913/12337	17 173/11960
no. parameters	660	585	657	652	585	648	640	648
2θ_max, deg	50.0	55.0	60.0	55.0	48.0	46.5	66.0	65.0
R1[b] [I > 2σ(I)]	0.0441	0.0316	0.0420	0.0477	0.0650	0.0281	0.0381	0.0349
wR2[c] [all data]	0.1198	0.0861	0.1290	0.0970	0.1873	0.0698	0.0989	0.0859

[a] Mo Kα radiation ($\lambda = 0.717\ 03$ Å) was used throughout. [a] $R1 = \Sigma||F_o| - |F_c||/\Sigma|F_o|$. [b] $wR2 = [\Sigma[w(F_o^2 - F_c^2)^2]/\Sigma[w(F_o^2)^2]]^{1/2}$ where $w = 1/\sigma^2(F_o^2) + (aP)^2 + bP$, $P = (F_o^2 + 2F_c^2)/3$.

mmol) of cobaltocene resulted in immediate formation of a dark-blue solution. This solution was stirred for 30 min and subsequently top-layered with Et_2O. After a few days, a mixture of dark-blue crystals of [Mn^III L^1_2]PF_6, bright-yellow crystals of [Cp_2Co]PF_6, and a minor amount of bright-red crystals [Mn^II L^0_2](PF_6)_2 were collected. The yellow [Cp_2-Co]PF_6 material was removed by washing the mixture with hot water (50 °C) until the water came off colorless. The red crystals of [Mn^II L^0_2]-(PF_6)_2 were removed by hand under a microscope. Yield: 260 mg (59%) of [Mn^III L^1_2]PF_6 as dark-blue/black crystals. FT-IR (KBr, cm^-1): 1629, 1605, 1582 (ν(C=N) + py- and aryl-ring deformations), 841, 558 (PF_6^-). Anal. Calcd for C_46H_46F_6MnN_6O_4P: C, 58.35; H, 4.90; N, 8.88; Mn, 5.80. Found: C, 58.19; H, 4.81; N, 8.74, Mn, 5.89.

6. [Fe^II L^0_2](PF_6)_2. Amounts of 0.20 g (1.57 mmol) of FeCl_2 and 0.60 g (1.61 mmol) of 2,6-bis[1-(4-methoxyphenylimino)ethyl]pyridine (L^0) were dissolved in 25 mL of MeOH, and the mixture was stirred at 20 °C for 30 min. Subsequently, 1.00 g (6.1 mmol) of NH_4PF_6 was added to the deep-purple solution, causing the precipitation of [Fe^II L^0_2]-(PF_6)_2 as a purple solid. The solid was collected by filtration, washed three times (10 mL) with ice-cold MeOH, air-dried, and recrystallized from CH_3CN/Et_2O. Yield: 808 mg (92% based on L^0 ligand) as purple/black crystals. FT-IR (KBr, cm^-1): 1604, 1582 (ν(C=N) + py- and aryl-ring deformations), 841, 558 (PF_6^-). ESI-MS, m/z: 947 [M − PF_6]^+,]^+, 401 [M − 2PF_6]^{2+}/2. Anal. Calcd for C_46H_46F_12FeN_6O_4P_2: C, 50.56; H, 4.24; N, 7.69; Fe, 5.11. Found: C, 50.42; H, 4.20; N, 7.73, Fe, 4.95.

7. [Ni^II L^0_2](PF_6)_2. Amounts of 0.24 g (0.82 mmol) of Ni(NO_3)_2·6H_2O and 0.51 g (1.37 mmol) of 2,6-bis[1-(4-methoxyphenylimino)-ethyl]pyridine (L^0) were dissolved in 20 mL of MeOH, and the mixture was stirred at 20 °C for 30 min. Subsequently, 1.00 g (6.1 mmol) of NH_4PF_6 was added to the brown solution, causing the precipitation of [Ni^II L^0_2](PF_6)_2 as a light-brown microcrystalline solid. The solid was collected by filtraion, washed three times (10 mL) with ice-cold MeOH, air-dried, and recrystallized from CH_3CN/Et_2O. Yield: 560 mg (74% based on L^0 ligand), as brown-black crystals. FT-IR (KBr, cm^-1): 1602, 1583 (ν(C=N) + py- and aryl-ring deformations), 841, 558 (PF_6^-). ESI-MS, m/z: 949 [M − PF_6]^+, 402 [M − 2PF_6]^{2+}/2. Anal. Calcd for C_46H_46F_12N_6NiO_4P_2: C, 50.43; H, 4.23; N, 7.67; Ni, 5.36. Found: C, 50.11; H, 4.15; N, 7.62; Ni 5.35.

8. [Cu^II L^0_2](PF_6)_2. Amounts of 0.20 g (0.83 mmol) of Cu(NO_3)_2·3H_2O and 0.30 g (0.80 mmol) of 2,6-bis[1-(4-methoxyphenylimino)-ethyl]pyridine (L^0) were dissolved in 20 mL of MeOH, and the mixture was stirred at 20 °C for 30 min. Subsequently, 1.00 g (6.1 mmol) of NH_4PF_6 was added to the brown solution, causing the precipitation of [Cu^II L^0_2](PF_6)_2 as a light-brown microcrystalline solid. The solid was collected by filtraion, washed three times (10 mL) with ice-cold MeOH, air-dried, and recrystallized from CH_3CN/Et_2O. Yield: 320 mg (72% based on L^0 ligand), as brown-black crystals. FT-IR (KBr, cm^-1): 1619, 1599, 1584(ν(C=N) + py- and aryl-ring deformations), 841, 558 (PF_6^-). ESI-MS, m/z: 954 [M − PF_6]^+, 404.5 [M − 2PF_6]^{2+}/2. Anal. Calcd for C_46H_46F_12N_6NiO_4P_2: C, 50.21; H, 4.21; N, 7.64; Cu, 5.77. Found: C, 50.06; H, 4.28; N, 7.67; Cu 5.85.

Supporting Information Available: Temperature-dependent magnetic susceptibility data (and fit) for [Cu^II L^0_2](PF_6)_2 (Figure S1), Mössbauer spectrum of [Fe^II L^0_2](PF_6)_2 at 80 K (Figure S2), the histogram of Mn−pyridine distances as compiled from the Cambridge Crystallographic Data Centre (Figure S3), and X-band EPR spectrum of [Fe^II L^0 L^1]^+ (Figure S4), tables of crystallographic and structure refinement data, atom coordinates and U_eq values, bond lengths and angles, anisotropic thermal parameters, and calculated and refined positional parameters of hydrogen atoms for complexes [ML_2](PF_6)_2 (M = Mn, Fe, Co, Ni, Cu, Zn) and [ML_2]PF_6 (M = Mn, Co), and eight X-ray crystallographic files in CIF format. This material is available free of charge via the Internet at http://pubs.acs.org.

IC000113J